Deep, shallow and surface fault-zone deformation during and after the 2021 Mw7.4 Maduo, Qinghai, earthquake illuminates fault structural immaturity

Dezheng Zhao[1], Chunyan Qu[*1], Roland Bürgmann[2], Xinjian Shan[1], Tao Li[1], Chenglong Li[1], Han Chen[1], Wenyu Gong[1]

[1]State Key Laboratory of Earthquake Dynamics, Institute of Geology, China Earthquake Administration, Beijing, 100029, China

[2]Department of Earth and Planetary Science and Berkeley Seismology Lab, University of California, Berkeley, CA94708, USA

* Contact author: Chunyan Qu (dqchy@ies.ac.cn)

Key Points

1. Detailed characteristics of fault-zone structure and kinematics of the 2021 Maduo earthquake
2. A more comprehensive quantification of deep, shallow and surface deformation features
3. We reveal inherent connections among immature fault zones, behaviors and strain budget

Abstract

Long-term fault growth involves the dynamic evolution of fault zone architecture, structural maturity, and physical properties. Accurate characterization of these features is essential for improved understanding of fault mechanics, rupture dynamics and earthquake hazard. Fault structural maturity has traditionally been quantified via analysis of geological features. Nonetheless, the manifestations of an incipient fault are still poorly known, partly due to a lack of fault outcrops and limited diagnostic characteristics of this type of fault. In this study, we integrate coseismic and postseismic geodetic (InSAR/GPS) observations, relocated aftershocks, optical satellite imagery, and field measurements to characterize the fault kinematics of the May 21 2001 Mw7.4 Maduo earthquake, which occurred on an immature fault. Using relocated aftershocks, we determine the fault damage zone thickness and damage density decay at a comparable resolution with field geological investigations. We analyze surface inelastic strain along the rupture using both InSAR and optical images. We construct a buried slip model and refine the coseismic slip distribution to determine a shallow slip deficit, which we attribute to off-fault deformation. We also examine the afterslip distribution and moment release following the earthquake to probe its relationship with coseismic rupture. All pieces of evidence point to the dominant role of immaturity of the fault hosting the Maduo earthquake. Our study demonstrates that the combined analysis of seismological data, geodetic observations and field measurements helps to comprehensively characterize fault structural maturity and to better understand the role of single earthquakes in the long-term fault zone evolution.

Plain language summary

Fault structural maturity controls its important physical properties, which evolve through long-term fault growth processes. These physical proprieties can be quantified and are useful to better understand regional earthquake hazards. However, due to the lack of geological outcrops and limited diagnostic characteristics at the surface, these important properties of the immature faults are poorly known. In this study, we use geodetic (InSAR/GPS) observations, relocated aftershocks, and optical satellite imagery, combined with field measurements to characterize the fault kinematics of the May 21 2001 Mw7.4 Maduo earthquake. This earthquake occurred on an immature fault on the Tibetan plateau and provides an opportunity to study deep, shallow and surface fault-zone deformation during and after the earthquake. We rely on kinematic models to characterize the deep fault structure and the relationship between deep and surface slip. Our comprehensive analysis provides a macroscopic description and characterization of the fault structure for the Maduo earthquake, at a resolution that can be directly compared to the geological studies

using field observations of exhumed faults.

1. Introduction

The pattern of earthquake slip distributions is significantly controlled by along-strike variations in fault properties, such as roughness, compliance, frictional strength, and fault segmentation separated by geometrical complexities (e.g., **Manighetti et al., 2015; Perrin et al., 2016; Savage and Brodsky, 2011**). These dynamically evolved properties relate to fault structural maturity with increasing total accumulated displacement (net slip) on a fault during its long-term growth (**Faulkner et al., 2011; Perrin et al., 2016**). However, the role of individual earthquakes in the long-term fault zone evolution is largely unknown.

Earthquakes generate permanent damage zones both deep in the crust and at the surface, producing wide-spread fractures and subsidiary faults at various scales. The permanent damage zones feature a nested hierarchical architecture, composed of one or multiple high-strain slip surfaces (the fault core) nested within a densely fractured, brecciated zone (the inner damage zone) and a much broader zone with distributed secondary faults (the outer damage zone) (e.g., **Manighetti et al., 2015; Perrin et al., 2016**). Geological and geophysical evidence suggests that the width of the outer damage zone is approximately 10% of the length of the active fault and tends to increase towards the lengthening direction of a parent fault (e.g., **Perrin et al., 2016; Shelef and Oskin, 2010**). Hence, damage zones are typically narrower along more mature larger-scale segments than along their more immature counterparts, corresponding to various levels of localization of the faults.

Fault maturity has been suggested to govern the magnitude, pattern and extent of surface inelastic failure during an earthquake, informed by geodetically mapped coseismic strain drawing on high-resolution optical imagery (e.g., **Barnhart et al., 2020; Cheng and Barnhart, 2021; Milliner et al., 2021** and many others). There is evidence that the width of the near-surface inelastic deformation zone, displays no diagnostic correlation with lithology, surface offset distributions and off-fault deformation (OFD) during an earthquake, but likely scales with the cumulative fault slip (net slip, **Cheng and Barnhart, 2021**). Permanent yielding of the host rocks in the surrounding crust is generated by stress concentrations at the dynamically propagating rupture tip during an earthquake. The resultant inelastic strain zone narrows with increasing rupture velocity, which tends to increase on more mature fault segments (**Barnhart et al., 2020; Perrin et al., 2016; Savage and Brodsky, 2011**).

Measurements of coseismic surface strain and OFD indicate the magnitude, extent, and spatial distribution of inelastic strain, which potentially helps to better quantify shallow fault slip and shallow slip deficit (SSD) during an earthquake. The apparent SSD, found in distributed slip models of some earthquakes, has been attributed to various mechanisms, including the inelastic yielding of the host rock near the surface (e.g., **Antoine et al., 2021**; **Barnhart et al., 2020**) and the presence of distributed OFD (e.g., **Kaneko and Fialko, 2011**). However, SSD is not an unambiguous phenomenon in all surface-rupture earthquakes and possibly depends on the earthquake magnitude (e.g., **Cheng and Barnhart, 2021; Lauer et al., 2020**). Detailed quantification of surface strain, OFD and SSD are of importance to probe the fundamental fault-slip physics related to near-surface rupture.

For the deep damage zone, seismicity distributions inform us of the geometry of faults and fault zone structures and have therefore been applied to characterize the damage zone thickness around active faults (e.g., **Powers and Jordan, 2010; Rodriguez Padilla et al., 2022; Savage and Brodsky, 2011; Valoroso et al., 2014**). Integrating both near- and far-field surface deformation observations and aftershock catalog helps us to better quantify elastic and inelastic deformation at various depths during an earthquake and to inspect the relationship between the deep damage zone and surface inelasticity.

The 2021 Mw7.4 Maduo earthquake struck the interior of the Bayanhar block on the northeastern Tibetan plateau, near the big bend of the Kunlun fault to the north of the epicenter (**Fig. 1**). Previous studies have constrained the fault geometry and coseismic slip distributions (e.g., **Guo et al., 2021; He K. et al., 2021; Wang, W. et al., 2021**), mapped coseismic and early postseismic deformation (**He L. et al., 2021; Jin and Fialko, 2021; Wang, W. et al., 2021**), documented the rupture kinematics on the surface (**Yuan et al., 2021**), and examined the strain accumulation constrained by pre-event geodetic observations (e.g., **Zhao et al., 2021**). The structural immaturity of the causative fault of the Maduo earthquake has been inferred based on an apparent SSD (~30%, **Jin and Fialko, 2021**), distributed interseismic shear strain (**Zhao et al., 2021**), and a mixed-mode of surface-breaking rupture and buried near-surface slip (**Yuan et al., 2021**).

Despite extensive efforts to understand the earthquake-cycle fault kinematics and the processes during and after the earthquake, a comprehensive picture of deep fault structure, the relationship between deep and surface slip, and the factors responsible for surface inelasticity and SSD are still lacking. In this study, we construct detailed images of fault zone structure, characterize the co-seismic surface strain and OFD, refine coseismic slip models, assess the buried shallow fault slip, and investigate the postseismic deformation processes after the Maduo earthquake by integrating all available geodetic (InSAR, GPS and optical images), seismological and field measurements.

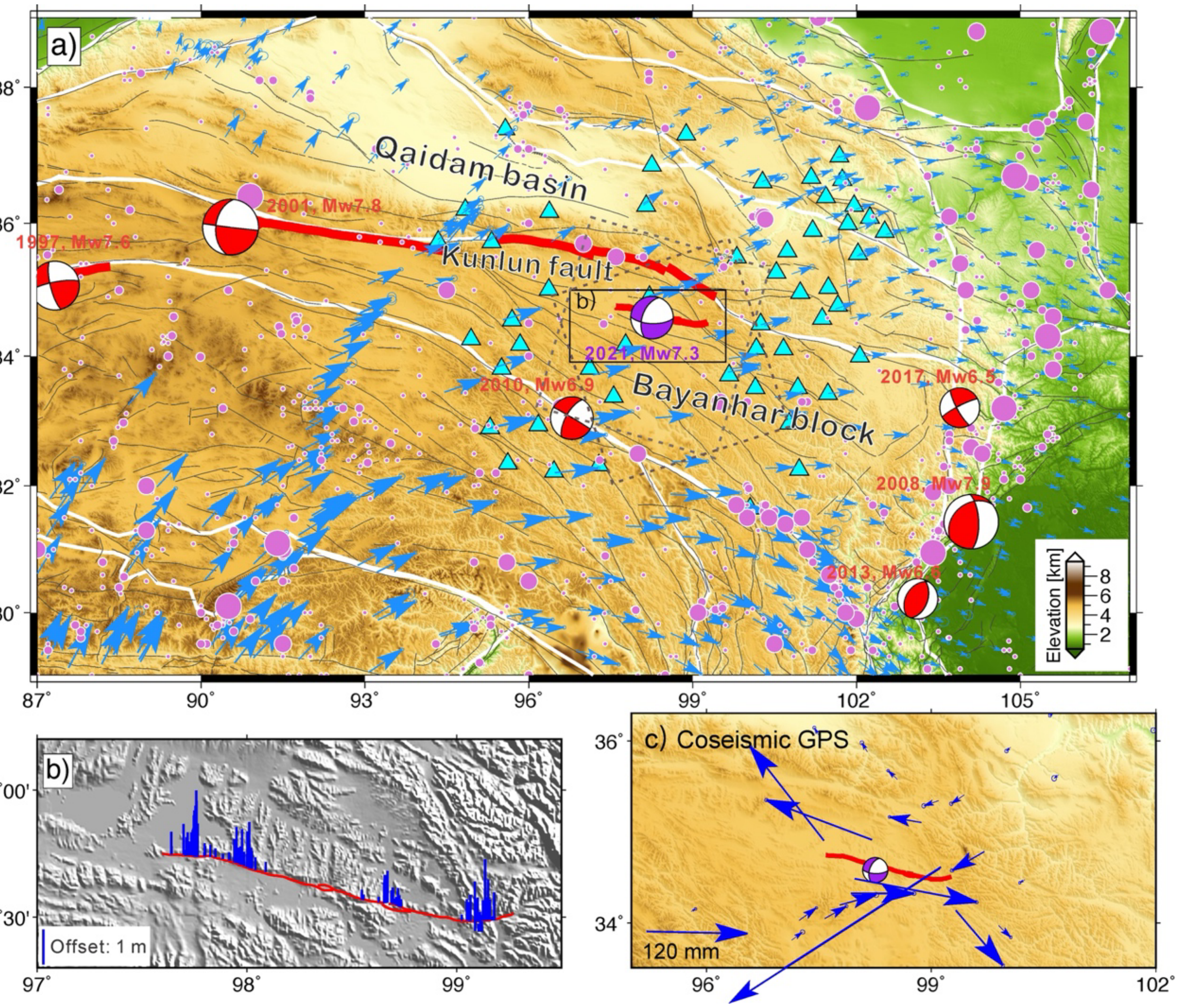

Figure 1. (a) Tectonic setting of the 2021 Mw7.4 Maduo earthquake. White lines denote major block boundaries on the Tibetan plateau. Thin grey lines show compiled active faults from **Taylor and Yin (2009)**. Light blue arrows indicate interseismic GPS velocity measurements in the Eurasia-fixed reference frame (**Wang and Shen, 2020**). Pink dots illustrate historical earthquakes with M>5 spanning the period of 1970-2016 from the USGS NEIC catalog. Red lines mark surface ruptures of the major historical earthquakes that occurred on the boundary faults of the Bayanhar block. Dashed rectangles display spatial extent of ascending and descending InSAR observations spanning the Maduo earthquake rupture. Cyan triangles are the seismic stations used to relocate aftershocks of the Maduo earthquake (**Wang, W. et al., 2021**). (b) Horizontal coseismic offsets of the Maduo earthquake measured in the field (**Yuan et al., 2021**) with surface rupture trace shown by red lines. (c) Coseismic GPS observations from **Wang et al., (2021)**.

2. Data

2.1 InSAR and GPS data

The coseismic interferograms on ascending and descending tracks have been published in **Zhao et al. (2021)**, **Jin and Fialko, (2021)** and many other previous studies. In this study, we focus on documenting the postseismic deformation following the Maduo earthquake using InSAR data. We collect the postseismic C-band (5.6 cm wavelength) Sentinel-1 SAR images acquired on two tracks with a repeat interval of 6/12 days, 11 radar images on ascending track 99 and 18 radar images on descending track 106 (**Fig. 1a**). Data from both tracks span the period from 2021/05/26 to 2021/09/11, nearly 3.5 months (108 days) after the mainshock.

We incorporate coseismic horizontal GPS displacements (**Fig. 1c**) from **Wang M. et al. (2021)**. The coseismic GPS displacements recorded at 58 continuous stations are widely distributed over a 300 km × 250 km area. For the GPS coseismic displacements, only minor contributions from postseismic deformation are included, which is estimated to be <1% three days after the mainshock at the near-field stations (< 50 km away from the fault; **Wang M. et al. 2021**). To the best of our knowledge, no postseismic (especially in the near-field of the fault) GPS observations have been published for the Maduo earthquake.

2.2 Surface crack mapping

The coseismic surface fracture dataset used in this study is from **Yuan et al. (2021)**. These cracks are visually interpreted, mapped and carefully digitized on a post-earthquake orthorectified photo mosaic with a high resolution of 4-8 cm acquired by VTOL fixed-wing UAV (unoccupied aerial vehicle), featuring a practical limit of the resolution for the Maduo earthquake (**Fig. 2a**). The ground cracks are classified into two categories based on location and distribution (**Yuan et al., 2021**). We calculate the azimuth of these cracks and investigate their distributions along different segments (**Fig. 2d**). The absolute accuracy of the locations of the cracks is estimated to be 20-40 cm (5 pixels). We also used the field-measured coseismic offsets on the surface to calculate the OFD during the Maudo earthquake (see **Section 3.4; Fig. 1b**).

The first category is related to the coseismic surface rupture belt along the causative fault, which forms a quasi-continuous surface trace along multiple segments and features an *en échelon* mixed-mode pattern. These cracks typically have orientations at small angles from the main surface rupture, indicating a dominant component of shear. The second category consists of widely distributed secondary cracks triggered by dynamic ground shaking during rupture, which are fully covered by UAV images (**Fig. 2a**). Most cracks of the second category are subparallel with river valleys covered by thick sediments and/or topographic contours, which produce a distinct azimuth distribution compared to the first classification (**Fig. 2d**).

2.3 Optical images

We use eight optical Sentinel-2 optical images with a resolution of 10 m to measure coseismic horizontal surface motion including east-west and north-south components for the Maduo earthquake. Due to significant cloud cover in the high plateau during summer and autumn, four post-earthquake images on track 47 were acquired on 2021/07/19, ~2 months after the earthquakes. Four suitable pre-earthquake images on track 47 were acquired on 2019/07/25, 2019/07/30, 2020/09/02, and 2021/03/01, respectively. The same incidence angles (~10° for the pre- and post-earthquake images) facilitate the mitigation of topographic distortions stemming from the parallax effect between multiple viewing geometries. No major earthquakes (Mw > 5) are reported in the Maduo area during 2019-2021/05/01 and the interseismic strain rate is estimated to be low (e.g., **Zhao et al., 2021**). Therefore, pre-earthquake images during 2019-2021 can be adopted as a reference for subpixel image correlation.

The pre- and post-earthquake Sentinel-2 orthoimages are correlated using the MicMac package (**Rosu et al., 2015**). The correlation results can be improved by using a smaller sliding window and a smaller correlation step, well suited for images with a high spatial resolution. To adequately suppress noise and decorrelation, we apply a sliding window of 3 × 3 pixels, a step of one pixel and a regularization term of 0.5, which result in a correlation map of 10 m in pixel resolution (**Rupnik and Daakir, 2017; Rosu et al., 2015**). We ultimately obtain the offset measurements in east-west and north-south directions, with an accuracy of approximately 1/20 of the pixel size. Given the resolution of 10 m for Sentinel-2 images, our pixel correlation allows detection of horizontal pixel motion of about 0.5 m. The correlation results are further processed by removing values with a normalized cross-correlation coefficient of <0.7. We evaluate the consistency between displacements projected into the line-of-sight (LOS) from the east-west and north-south components of the optical image offsets and the InSAR observations, shown in **Fig. S6**. The image offset and InSAR LOS displacement estimates agree to within 0.3 m and 0.15 m (2 standard deviations) for the ascending and descending SAR orbit acquisitions, respectively (**Fig. S6**).

2.4 Relocated aftershocks

We employ the relocated aftershock catalog (**Wang, W. et al., 2021**) from May 25, 2021 to June 7, 2021, 14 days after the May 21, 2021 Mw7.4 mainshock, with 7138 events in the area around the causative fault (**Fig. 2b**). The catalog is generated using the double difference algorithm hypoDD (**Waldhauser, 2020**), which has the capability of suppressing the location error due to lateral inhomogeneity of the crustal velocity structure. Overall, the average location errors of relocated aftershocks for latitude, longitude, and depth are 0.27, 0.24, and 0.50 km, respectively (**Wang, W. et al., 2021**). To calculate the spatial density of the relocated aftershocks, we utilize 0.05° grid elements and extract all available events within the grid (**Fig. 2c**).

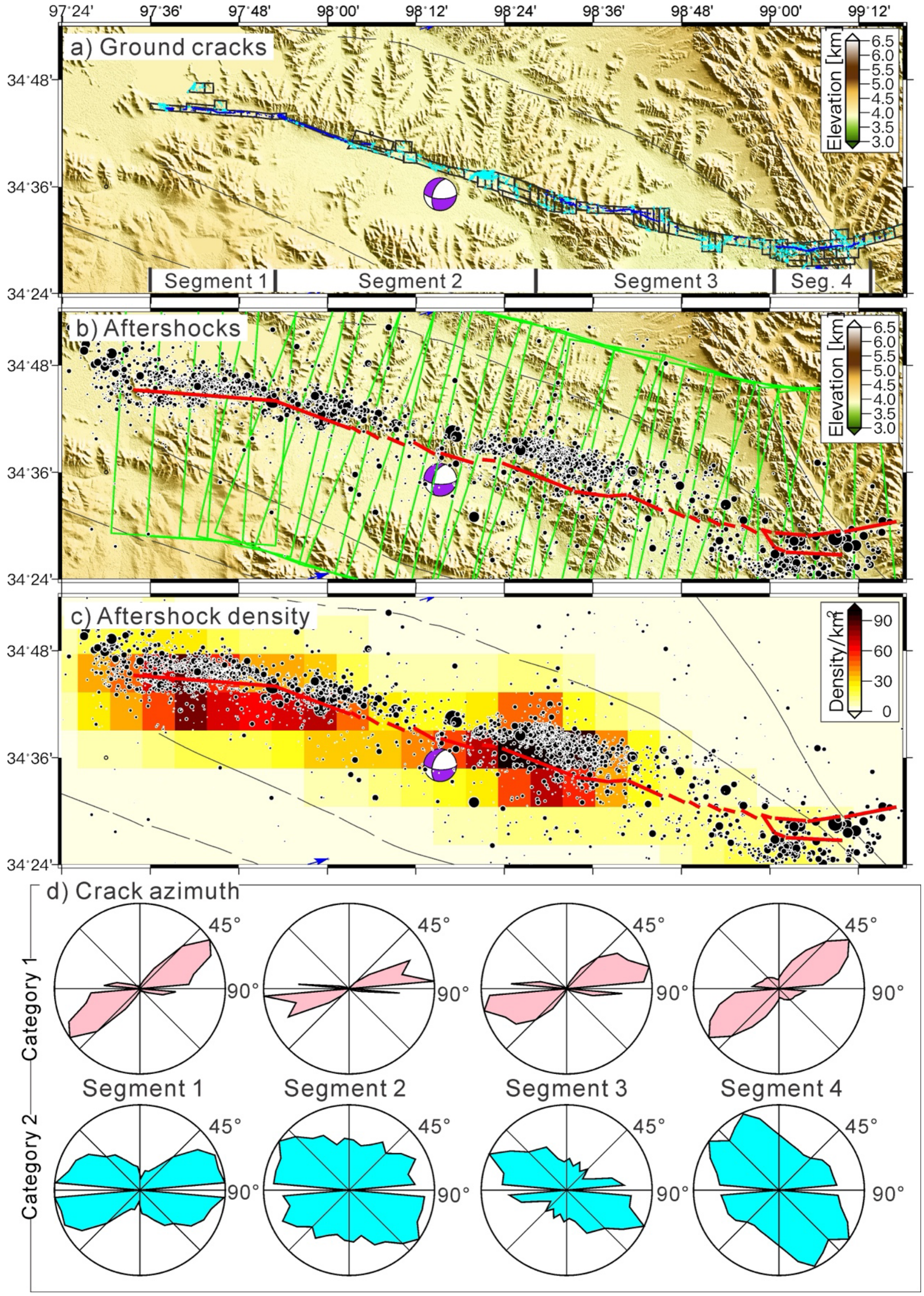

Figure 2. (a) Two categories of ground cracks associated with the Maduo earthquake (**Yuan et al., 2021**). Blue lines are the first category associated with the relatively continuous main fault rupture zone, which are trackable in the field. Cyan lines mark the more widely distributed ground cracks around the main fault rupture zone and along some segments with buried fault slip. Gray polygons are the footprint of the UAV images. (b) Distribution of relocated aftershocks, displayed by black dots. Green lines are surface projections of 20 northeast-oriented, 20-km-long, 5-km-wide vertical boxes used to calculate the deep damage zone thickness, and damage density decay. Red lines are surface displacement discontinuities interpreted from InSAR observations, shown in **Fig. 3**. (c) Distribution of aftershock density along the length of the rupture, highlighting two main clusters of aftershocks. (d) Rose diagrams showing the orientation of two categories of ground cracks along four segments from west to east along the rupture shown in (a). The pink petals correspond to the first category of ground cracks (blue lines in a), and cyan petals are related to the second category of ground cracks (cyan lines in a).

3. Methods

3.1 Post-seismic InSAR displacement

We utilize the InSAR Scientific Computing Environment (ISCE, version 2) software (**Rosen et al., 2012**) and the persistent scatterer (PS) method implemented in the Stanford Method for Persistent Scatterers (StaMPS version 4.1b; **Hooper et al., 2012**) to mitigate atmospheric and other types of phase noises, and calculate the postseismic displacement time series of identified stable PS points (**see supplement for full methods description**).

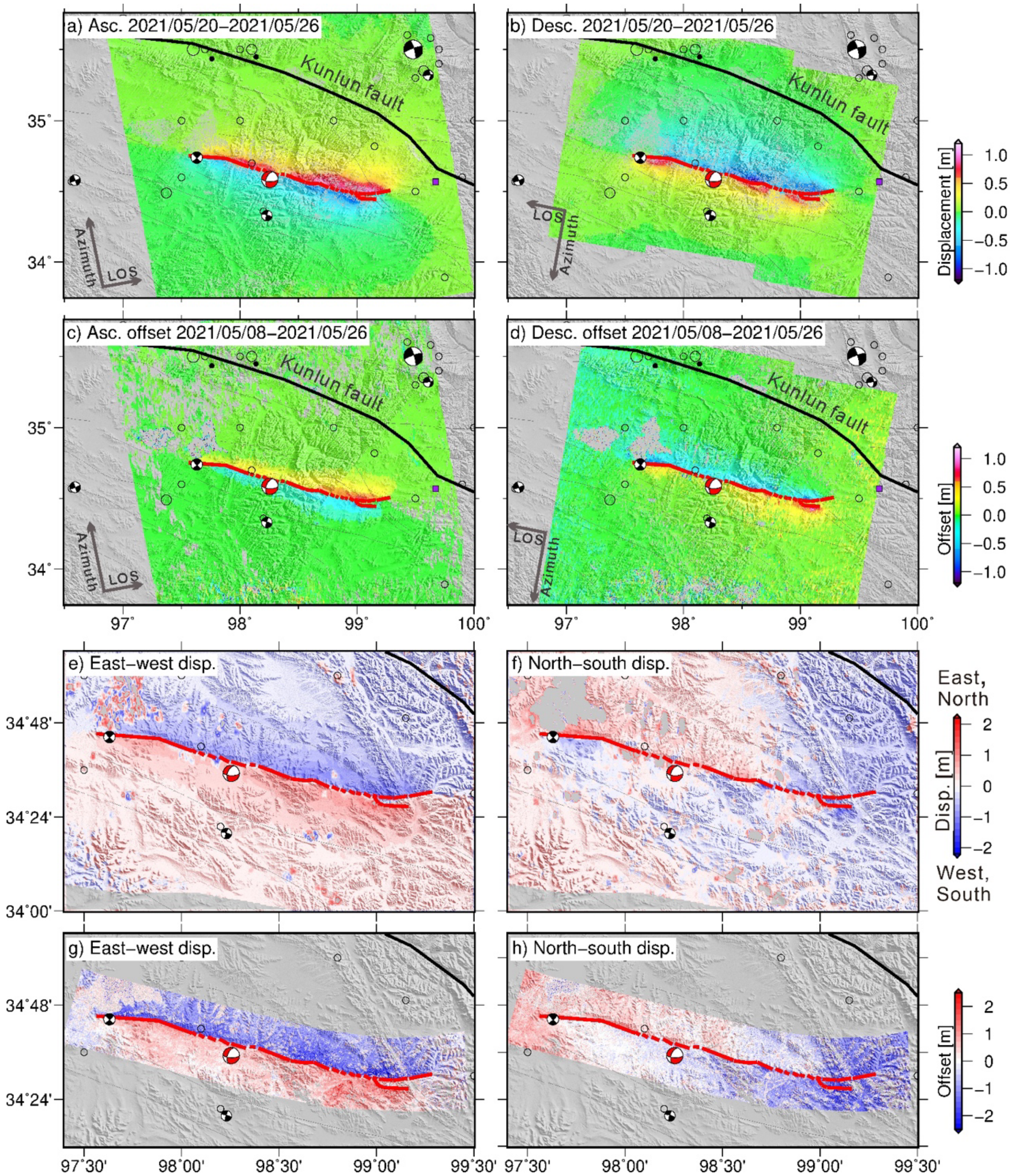

Figure 3. Line-of-sight (LOS) coseismic displacements from Sentinel-1 InSAR (a, b), range offsets from offset tracking of Sentinel-1 images (c, d), the reconstructed horizontal displacement components from InSAR (e, f), and optical image offsets (g, h) due to the 2001 Mw7.4 Maduo earthquake. In LOS/range displacements (a-d), positive values correspond to surface movement toward the satellite. The focal mechanism (in red) of the Maduo earthquake is marked. Red lines illustrate surface rupture traces based on the interpretations of InSAR near-field phase gradients. Black lines in northeast corner denote the Kunlun fault.

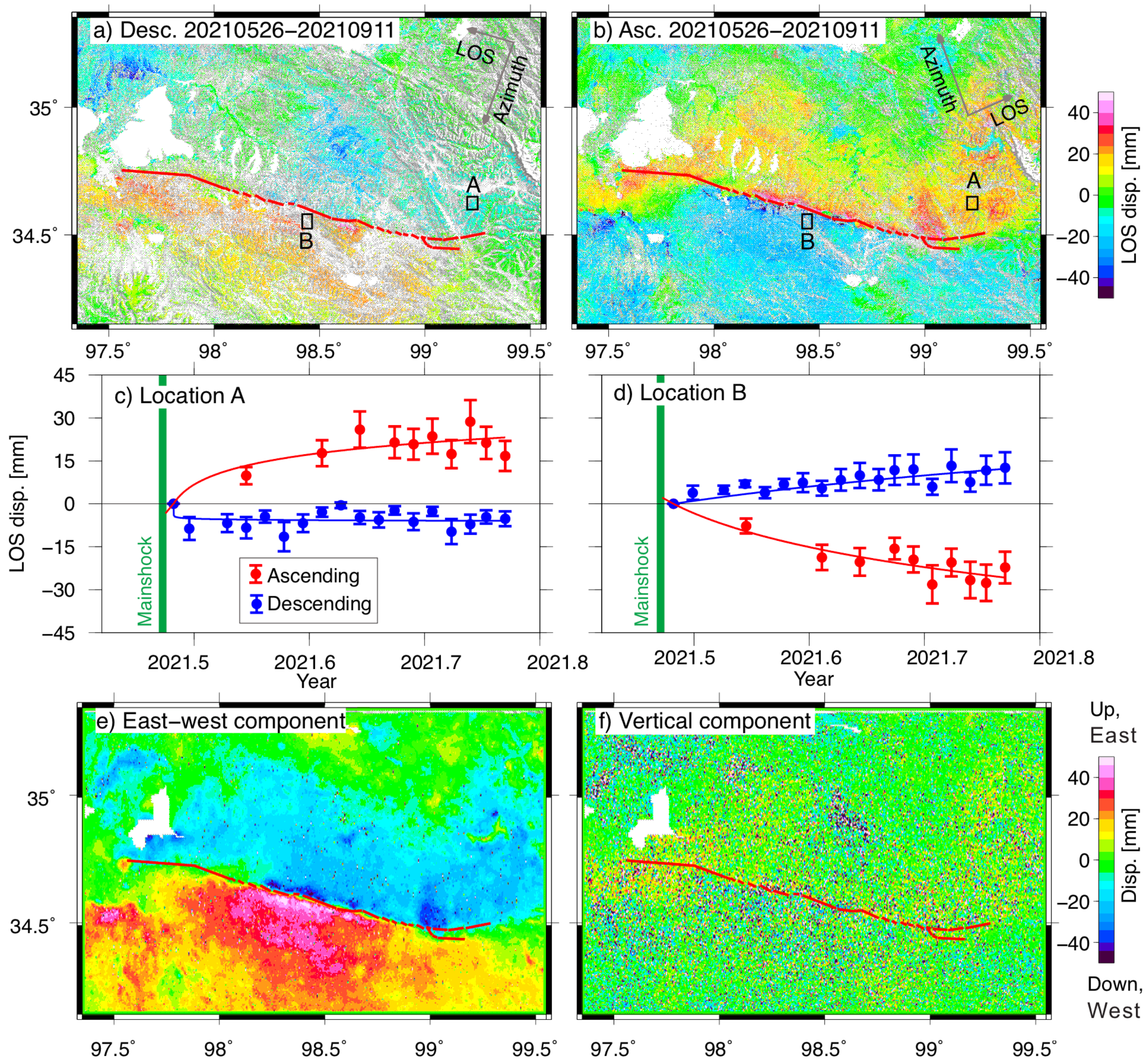

Figure 4. (a, b) Cumulative postseismic InSAR displacements on the ascending and descending tracks following the Maduo earthquake, spanning 2021/05/26 to 2021/09/11. (c, d) LOS displacement time series of ascending (red dots) and descending (blue dots) observations at locations A and B, shown in (a, b). The solid curves represent line fittings using a logarithmic decay function, $D(t) = a + b \times log\left(1 + \frac{t-t_0}{\tau}\right)$, where the postseismic displacement, $D(t)$, evolves as a function of the acquisition time of SAR images (t), the time of the earthquake (t_0) and a characteristic relaxation time (τ). (e, f) demonstrate the decomposed east-west and vertical postseismic displacement components derived from the 108-day cumulative LOS displacements, respectively.

3.2 Analysis of deep damage zone thickness, damage density decay and seismic potency

The relocated aftershock catalog of the Maduo earthquake (**Wang, W. et al., 2021**) helps to illuminate geometry and properties of the deep fault structure at a scale of kilometers to several hundreds of meters, comparable to field geological investigations (e.g., **Savage and Brodsky, 2011; Valoroso et al., 2014**). We divide the aftershock zone into 20 northeast-oriented, 20-km-long, 5-km-wide vertical boxes (**Fig. 2b**). In each profile box, we construct a histogram associated with the distribution of the number of aftershocks around the fault plane (**Fig. S1**). These histograms are statistically characterized by a normal distribution centered at the modelled fault plane. We follow the method proposed in **Valoroso et al. (2014)** to describe the deep damage zone thickness (DDZT) as 2 standard deviations of the aftershock distribution, which includes 95% of the aftershocks and reflects the localization and diffusion of aftershocks. We calculate the decay of the aftershock density, indicated by the number of earthquakes occurring every 200 m perpendicular to the modelled fault plane, as a power-law function (d^{-n}) of distance (d) from the fault (e.g., **Savage and Brodsky, 2011**; **Fig. S1**). The decay of the number of near-field aftershocks is correlated with the decaying intensity of deformation in the deep (inner and outer) damage zones from the fault core into nearby regions composed of relatively undeformed rocks.

We quantify the size of aftershocks using the scalar seismic potency ($P_0 = \int_A s\, dA,$) associated with the integral of slip (s) over the rupture area (A) (e.g., **Ben-Zion, 2008**). The calculation is achieved based on the quadratic potency-magnitude scaling relations of **Ben-Zion and Zhu (2002)**.

3.3 Coseismic slip and afterslip models

The fault geometry and coseismic slip distributions of the Maduo earthquake have been extensively investigated using GPS and/or InSAR data (e.g., **Guo et al., 2021; He L. et al., 2021; He K. et al., 2021; Jin and Fialko, 2021; Wang M. et al., 2021; Zhao et al., 2021**). These models highlight a multi-segment rupture with several concentrated slip patches, separated by structural complexities that may have acted as barriers during rupture propagation. However, the determined slip distributions are inevitably influenced by the imposed fault geometry, discretization, parameterization, regularization, and variable types of data constraints in the inversion.

In this study, we jointly employ coseismic InSAR observations and horizontal GPS displacements to invert for the coseismic slip distributions using the steepest descent method (SDM, **R. Wang et al., 2013**), implementing a linear inversion method, Sensitivity Based Iterative Fitting (SBIF). Details associated with the calculation of Green's functions, fault discretization, data resampling and inversion strategy can be found in **the supplement**. To investigate the effect of the data completeness in the near-field of the fault on the shallow slip distribution, we also add the east-west and north-south displacement components from the image-offset data in the inversion using the SDM method (**R. Wang et al., 2013**).

To explore the potential influence from fault discretization, model parameterization, and regularization during the inversion, we further generate two additional slip models following the methodology of **Fialko (2004)** and **Amey et al. (2008) (see supplement for full methods description)**. All the coseismic slip models use the same fault geometry, allowing for a self-consistent comparison. The similarities and discrepancies between our three coseismic slip models provide useful clues for assessing the ability of the kinematic models to resolve the coseismic slips at various depths and along different segments during the Maduo earthquake. We calculate the root mean square (RMS) values to compare the different models. We also compile the published slip models from **He L. et al. (2021), He K. et al. (2021) and Jin and Fialko, (2021)** for a comparison. These models are all based on similar coseismic geodetic datasets but with varied inversion methodology, fault geometry and regularization.

For the afterslip modeling, we use the cumulative postseismic displacements (**Fig. 4**) obtained from the InSAR images to constrain afterslip distributions under the assumption that the majority of the postseismic deformation is generated by afterslip on the fault plane. We utilize an identical fault geometry as for coseismic models in the inversion. Because afterslip generally extends deeper than the coseismically ruptured area, we expand the base depth of the fault to 25 km to capture deep afterslip. The fitted ground displacements are plotted in supplementary materials (**Fig. S14**).

3.4 Coseismic fault-parallel offset, surface strain and OFD calculations

We invert a series of fault-parallel displacement swath profiles for the total across-fault offset (T), the fault location (c), the shear-zone width (W_s), the strain (ε_{el}) and the constant intercept (a) using the following function (**Milliner et al., 2021**):

$$y(x) = \frac{T}{2} \cdot \mathrm{erf}\left(\frac{x-c}{\sqrt{2}W_s}\right) + \varepsilon_{el} \cdot x + a \quad (1)$$

$$\mathrm{erf}(\mathrm{r}) = \frac{2}{\sqrt{\pi}} \int_0^r e^{-t^2}\, dt, \text{ with } \mathrm{r} = \frac{x-c}{\sqrt{2}W_s} \quad (2)$$

where x is the distance along each profile. We utilize a Bayesian sampling approach incorporating the affine-invariant ensemble Markov chain Monte Carlo (MCMC) sampler (**Goodman and Weare, 2010**) to search for the best fit solutions (T, c, W_s, ε_{el}, a), the full covariance and uncertainties of model parameters for each displacement profile. We generate 500 initial walkers to explore the parameter space and the model runs over 500,000 iterations to guarantee more than ten thousand independent random samples. We use the maximum *a posteriori* (MAP) solution to represent the best-fitting value for model parameters.

Based on the horizontal coseismic displacement maps from both InSAR and optical images, we calculate the shear, vorticity and dilatation strains using the method described in **Zhao et al. (2021)**. We form a series of shear strain swath profiles (5,000 × 500 m) spaced every 500 m along the fault rupture trace and compute the width of the areas with shear strain larger than the 0.2% of the shear strain intensity (magnitude of shear strain). Shear strain of 0.2% corresponds to the lower elastic limit of rocks, calculated as the mean ratio of yield stress to Young's modulus. These areas are expected to have permanent and unrecoverable inelastic strain. We find that the maximum shear strain measured along the entire rupture of the Maduo earthquake remains below the maximum elastic strain, 0.5% (e.g., **Lockner, 1998; see analysis further below**).

Due to the fact that the coseismic rupture did not fully reach the surface along several segments (i.e., feature a buried near-surface slip front, **Fig. 2a**) and the observed distributed nature of fault displacement along several surface-rupturing segments during the Maduo earthquake, the on-fault displacement is difficult to measure in the field (see detailed description in **Yuan et al., 2021**). The total displacement is typically spread over >200 m distance from the fault (**Fig. S10**), and it is challenging to identify specific markers at the surface to measure on-fault displacement. Using limited on-fault offset measurements in the field (**Fig. 1b**), we calculate the OFD distribution at these locations.

3.5 Buried slip models

We invert the fault-parallel displacement profiles ($D(x)$) for potentially buried fault slip (s) using the analytical arctan solution for a 2D screw dislocation in a homogeneous elastic half-space between upper (d_2) and lower (d_1) dislocation depths (**Savage and Burford, 1973**):

$$D = \frac{s}{\pi}\arctan\left(\frac{x}{d_1}\right) - \frac{s}{\pi}\arctan\left(\frac{x}{d_2}\right) \quad (3)$$

We fix d_1 conservatively at 15 km to prevent edge effects and search for the best fit d_2 and s.

Rather than assuming the simple uniform-slip dislocation, a more physical model would include the gradual slip from shallower to deeper depth, albeit at the expense of more free parameters. To this end, we also apply the buried slip model incorporating a tapered slip distribution in the shallow subsurface, meaning that the constant slip, s, between the upper (d_2) and lower (d_1) dislocation depths, gradually decreases to zero at a much shallower depth (d_3) below surface. The fault-parallel offset profile (D) is approximatively obtained via the superposition of a suite of dislocations of coseismic slip in a homogeneous elastic half-space:

$$D = \sum_{j=0}^{N}\left[\frac{\Delta s_j}{\pi} arctan\left(\frac{x}{d_2 - j\Delta z}\right) - \frac{\Delta s_{j+1}}{\pi} arctan\left(\frac{x}{d_2-(j+1)\Delta z}\right)\right] + \frac{s}{\pi}\arctan\left(\frac{x}{d_1}\right) - \frac{s}{\pi}\arctan\left(\frac{x}{d_2}\right) \quad (4)$$

$$\Delta s_j = s(d_2 - (j+1)\Delta z) - s(d_2 - j\Delta z),\ j \geq 0;\ \Delta z = 0.2\ km \quad (5)$$

We only consider a linear decrease in the buried slip model when incorporating the tapered slip distribution updip of the uniform-slip dislocation. We use the aforementioned Bayesian sampling approach implementing the affine-invariant ensemble MCMC sampler (**Goodman and Weare, 2010**) to search for the best fit parameter related to the depth and slip amplitude for two models. We schematically demonstrate the difference between models without and with the tapered slip distribution in **Fig. 8a, 8b**.

4. Results

4.1 Deep damage zone thickness (DDZT) and damage density decay

Both the DDZT and the exponent of damage density decay exhibit clear variations along the rupture (**Fig. 5a, 5b**). We describe along-strike variations for two primary fault segments, separated by the epicenter, the eastern segment from longitude 98.4° to 99.3° and the western segment from 97.5° to 98.4°. Overall, the coseismic rupture generated a wide damage zone and the resolved DDZT ranges from 6 to 18 km, with greater values on the eastern segment (**Fig. 5a**). This feature is consistent with a larger amount of coseismic slip to the east of the epicenter constrained by coseismic geodetic observations between longitude 98.8° to 99.2° (e.g., **He L. et al., 2021; Jin and Fialko; Zhao et al., 2021; Fig. 10**), suggesting that larger coseismic slip on the eastern segment produced more wide-spread aftershocks compared to the western segment.

The large DDZT resolved here is likely associated with the triggered seismicity on the nearby fault strands in the outer damage zone. This inference is supported by the large portion of the aftershock zone that overlaps with the primary coseismic rupture zone, implying that coseismic rupture triggered aftershocks in the adjoining rock volumes (**Fig. 5**). Another factor leading to the obtained large DDZT values lies in the damage proxies in the formulation used in this study (Section 3.2). Compared to the aftershock density quantification used in **Rodriguez Padilla et al. (2022)**, our approach inherently incorporates more aftershocks in both the inner and outer damage zones.

We note that the spatial variation of the DDZT is not time-dependent (**Fig. 5a**). To examine the spatial variation of the DDZT, we also show the DDZT distribution for 4×4 km grid patches along the fault (**Fig. 5c**). We find that for the eastern segment, an insufficient number of aftershocks (mostly with a larger moment magnitude compare to the western segment) results in substantial data gaps. We find that the value of DDZT is relatively lower within and around the main rupture region along the western segment, and the thickness tends to be widened outside (**Fig. 5c**).

The exponent of damage density decay also illustrates along-strike changes in the range of 0.5-1 with relatively larger values along the western segment, indicating more localized aftershock distributions. No noticeable difference in the decay trend is identified between the hanging-wall and footwall sides of the fault (**Fig. 5b**). Additionally, the eastern and western segments are characterized by contrasting density distribution but comparable seismic potency, implying that fewer aftershocks with larger magnitude dominantly occurred along the eastern segment (**Fig. 5d-5f**). The DDZT and the exponent of damage density decay along the whole rupture are not correlated with the D95 depth extent of seismicity (**Fig. 5a**), aftershock density (**Fig. 5d**) and seismic potency of aftershocks (**Fig. 5e**).

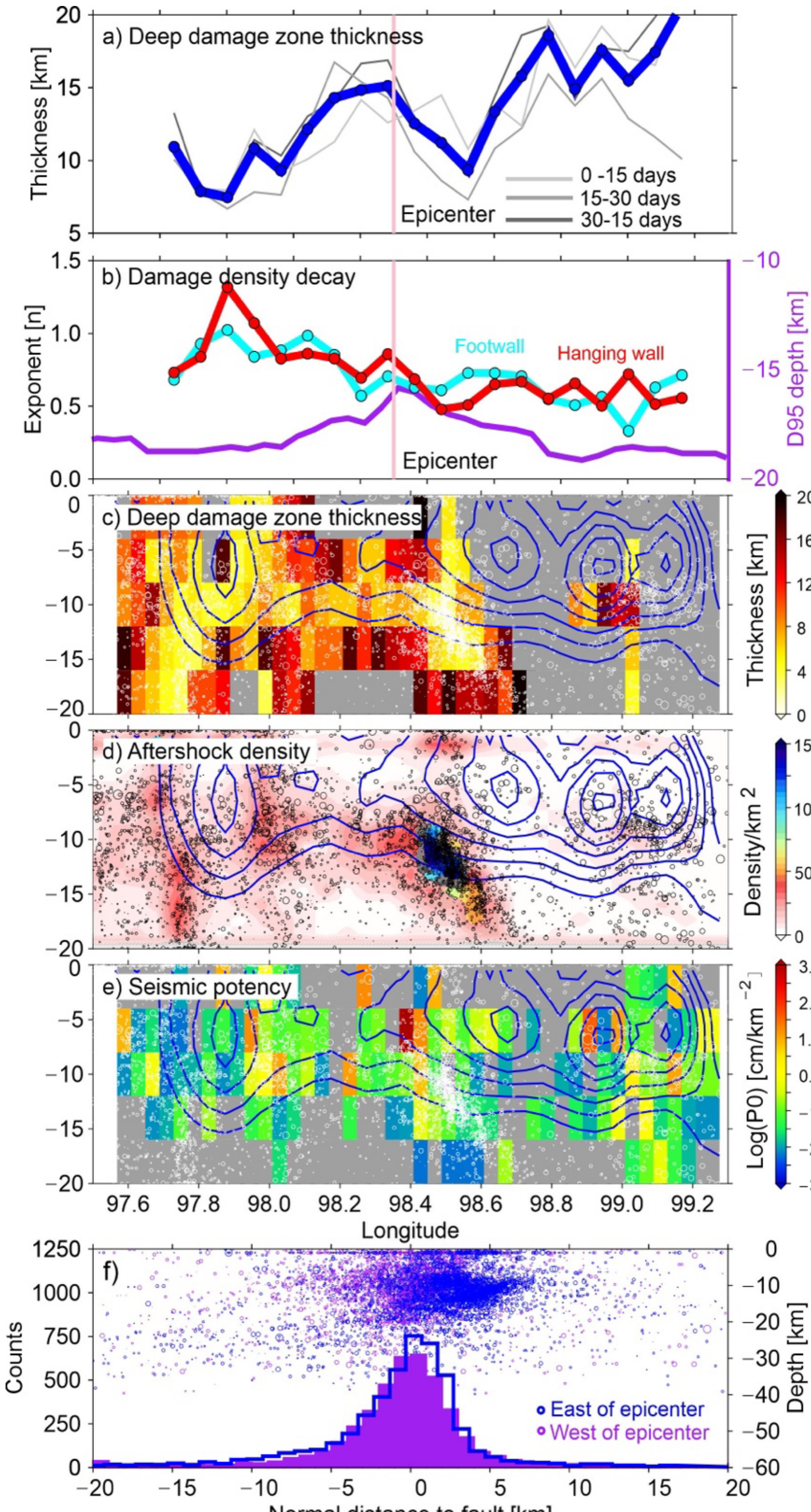

Figure 5. (a) Along-strike variations of thickness of the deep damage zone (blue line). (b) Variation of damage decay

exponent, n, for hanging-wall to the north (red line) and footwall to the south (cyan line). D95 depth (purple line) of aftershocks is estimated from a sliding window (20 km) along strike. Pink lines in (a, b) indicate the epicenter. (c) Distribution of the DDZT of deep damage zone on the fault plane, measured over grid of rectangular boxes with dimensions of 5 km and 4 km along strike and dip of the fault, respectively. Grey areas are volumes without enough number of aftershocks (<30) to provide statistically significant measurements. (d) Distribution of density of aftershocks on the fault plane. (e) Potencies of aftershocks along the fault. (f) Spatial distribution of aftershocks (point clouds) along the cross-fault distance (from south to north) and depth directions and histograms of number of aftershocks. Purple color denotes the selected aftershocks between longitude 97.5° and 98.4°, to the west of the epicenter and blue color indicates the aftershocks between longitude 98.4° and 99.3°, to the east of the epicenter.

4.2 Along-strike distributions of coseismic surface strain

We compute coseismic surface strain, including dilatation, vorticity and shear strain, and the second invariant (left panels in **Fig. 6**), using 10-m resolution displacement maps derived from subpixel image correlation (**Fig. 3g, 3h**). We compare these strain maps with InSAR-derived strain maps (right panels in **Fig. 6**) with a resolution of 90 m from **Zhao et al. (2021).** Both results are based on the same approach to invert for the displacement gradient and finite strain tensors, $E = \frac{1}{2}(\partial_x u_y + \partial_y u_x + \partial_x u_y \cdot \partial_y u_x)$.

The Maduo earthquake generated well resolved shear strain, $s = \frac{1}{2}(\partial_x u_y + \partial_y u_x)$, and vorticity, $\omega = \frac{1}{2}(\partial_x u_y - \partial_y u_x)$, along the surface ruptures (**Fig. 6**). Specifically, the shear strain exhibits maximum values ranging from 0.1% to 0.4% along different segments, which are all lower than the commonly assumed upper limit of 0.5% yielding strain of rocks. The localization and magnitude of shear and vorticity strain are spatially variable and are not visually identified at several locations of the central segment and towards the two ends of the coseismic rupture. These regions correspond to the surface rupture gaps, which have extremely low values of the second invariant of strain tensors (**Fig. 6**).

Another important feature is that the resolved dilatational strain from the optical images is insignificant and largely undetectable, but the InSAR-derived dilatation map displays observable, distributed zones of dilatation and contraction within a broader zone throughout the fault zone. Particularly, pronounced dilatational strain is found at the westernmost end of the rupture, consistent with the significant normal slip inferred from the coseismic slip inversion and field investigation (>0.5 m vertical displacements, about >40% of the horizontal displacement; **Fig. 6d;**

Yuan et al., 2022; Zhao et al., 2021). We speculate that InSAR observations are more sensitive to small-magnitude and potentially longer-wavelength deformation and thus have the ability to detect the subtle displacement gradient and more distributed dilatation strain during the Maduo earthquake. However, for InSAR measurements, the robustness of this subtle dilatation largely depends on the quality of coherence/unwrapping near ruptures and the accuracy of the NS component. That can be improved by additional constraints from range displacement measurements from SAR pixel offsets when resolving the three-dimensional displacement fields. Overall, the lack of localized dilatation strain in the Maduo earthquake is consistent with surface strain measurements associated with the 2019 Ridgecrest earthquake by Antoine et al. (2021) and Milliner et al. (2021). If the distributed dilatation strain is robust, the change in the sign likely results from the varied strike and dip of the fault plane, particularly along large releasing/restraining bends along the rupture (Milliner et al. 2021), which likely dominates the spatially variable dilatation strain.

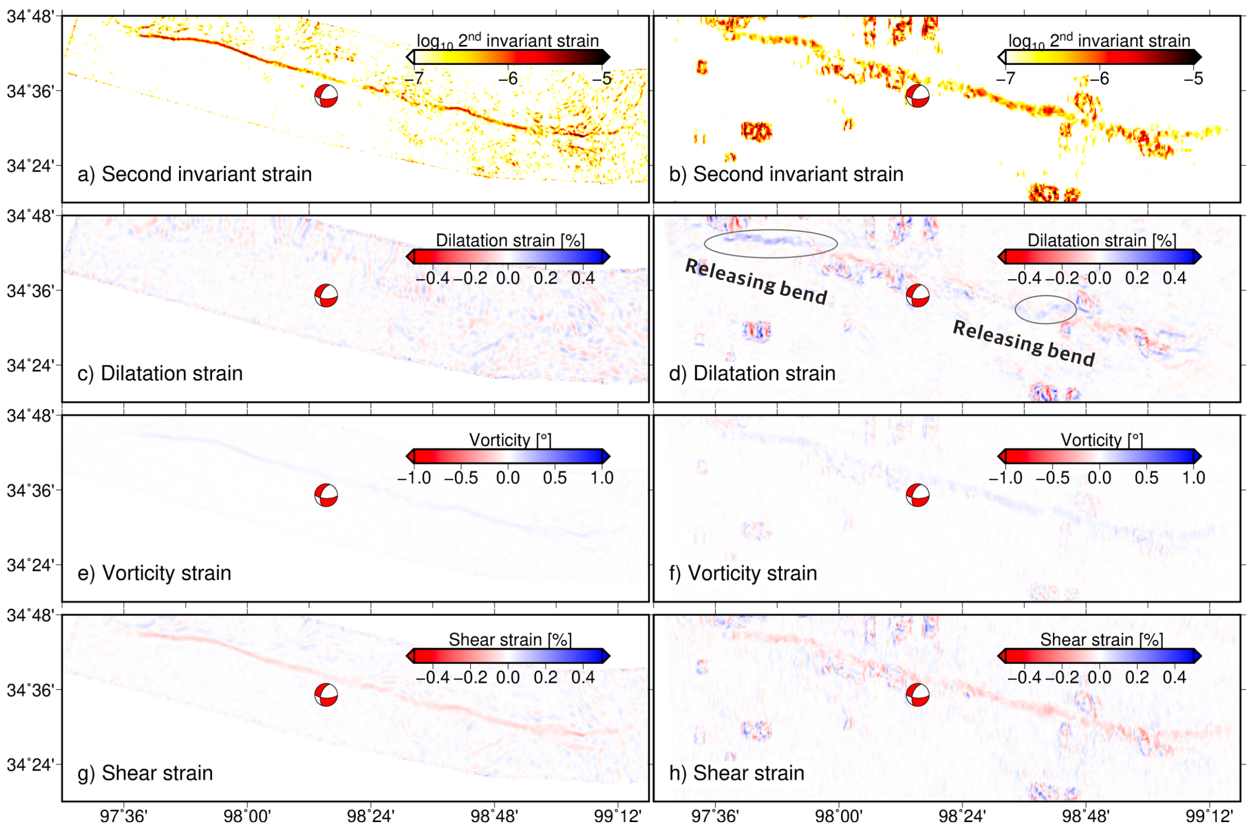

Figure 6. Strain maps derived from horizontal offsets using optical images (a, c, e, g) and from InSAR and offset-tracking derived horizontal components of coseismic displacements (b, d, f, h; Zhao et al., 2021). Beach ball shows the focal mechanism of the 2021 Maduo earthquake. The color scales of dilatation and shear strain saturate at ± 0.5%, which corresponds to the upper bound of the approximate yield strain measured for rocks in the laboratory

(e.g., **Lockner, 1998**).

4.3 Buried shallow slip front near the surface and SSD

The field investigations conducted immediately after the Maduo earthquake and the detailed mapping of ground cracks (**Figs. 1, 3**), along with analysis of aftershocks (**Fig. 2**) and strain maps from InSAR and optical image geodesy (**Fig. 6**), confirm that the coseismic rupture did not reach the surface along several segments (**Yuan et al., 2021**). Accordingly, we analytically invert for the depth and slip using a simple two-dimensional screw dislocation model with additional considerations of tapered slip. The two-dimensional elastic models incorporate the upper slip front, and they are not impacted by the choice of regularization and discretization in three-dimensional models when trying to resolve the SSD (**Xu et al., 2016**).

Our results (**Figs. 7**, **S7, S8**) suggest a strong consistency between fault segments with larger depth of the updip limit of coseismic slip and untraceable surface ruptures (**Fig. 7c**, **2**), such as the segment between longitude 98.1° and 98.6°. The inverted slip on the 2D dislocation is mostly less than 3 m, compared to deep slip (> 4 m) obtained in the coseismic slip distribution in three dimensional models (**Fig. 10**). This comparison reflects the inferred SSD (50% between 97.6°and 98.5°, 30% between 98.5°-99.4°). As expected, the predicted near-surface slip is in strong agreement with our deep coseismic slip distribution (**Fig. 10**). The maximum near-surface slip inferred from the 2D modeling occurs to the east of the epicenter. The depths of the updip limit of the buried slip front from models without and with incorporating a tapered shallow slip are also overall consistent (**Fig. 7c**). However, the tapered shallow slip model resolves a lower amount of shallow slip (**Fig. 7b,** <20%) at the expense of deepening the upper edge of the dislocation with deep constant slip (**Fig. 7c**). Our buried slip modeling confirms that the near-field displacement gradient (within ±4 km of the fault) analyzed above is associated with shallow slip and deformation and does not arise from elastic response associated with slip at large depths (>4 km; **Fig. S10**).

Despite reliable surface expressions of discontinuous *en echelon* fractures and mole tracks in the field (**Yuan et al. 2021; Fig. 2**), our model infers a spatially varied buried shallow slip front near the surface (0-4 km) for the Maduo earthquake. In the modelling, the simple elastic model without considering increasing inelastic failure at shallow depths would inherently bias the estimated depth of the buried slip front, however, the conspicuous buried slip front during the Maduo earthquake along several segments has been inferred in the field work (**Yuan et al., 2021**). Using the in-situ near-surface measurement of velocity structure and corresponding distribution of elastic properties (shear and Young's moduli, Poisson's ratio) in the mechanical models would lead to a greater slip at shallower depth, with more slip reaching the near-surface (e.g., **Nevitt et al., 2020**).

The buried slip front may help to explain the pattern of the localized shear but more distributed dilatation strain (**Fig. 6**), due to the fact that processes related to area-conserving distortion (shear) tend to be localized in a limited zone, whereas dilatation exhibits deformation over a broader distance. In particular, in the cases of a buried slip front, the surface dilatation is expected to be more distributed.

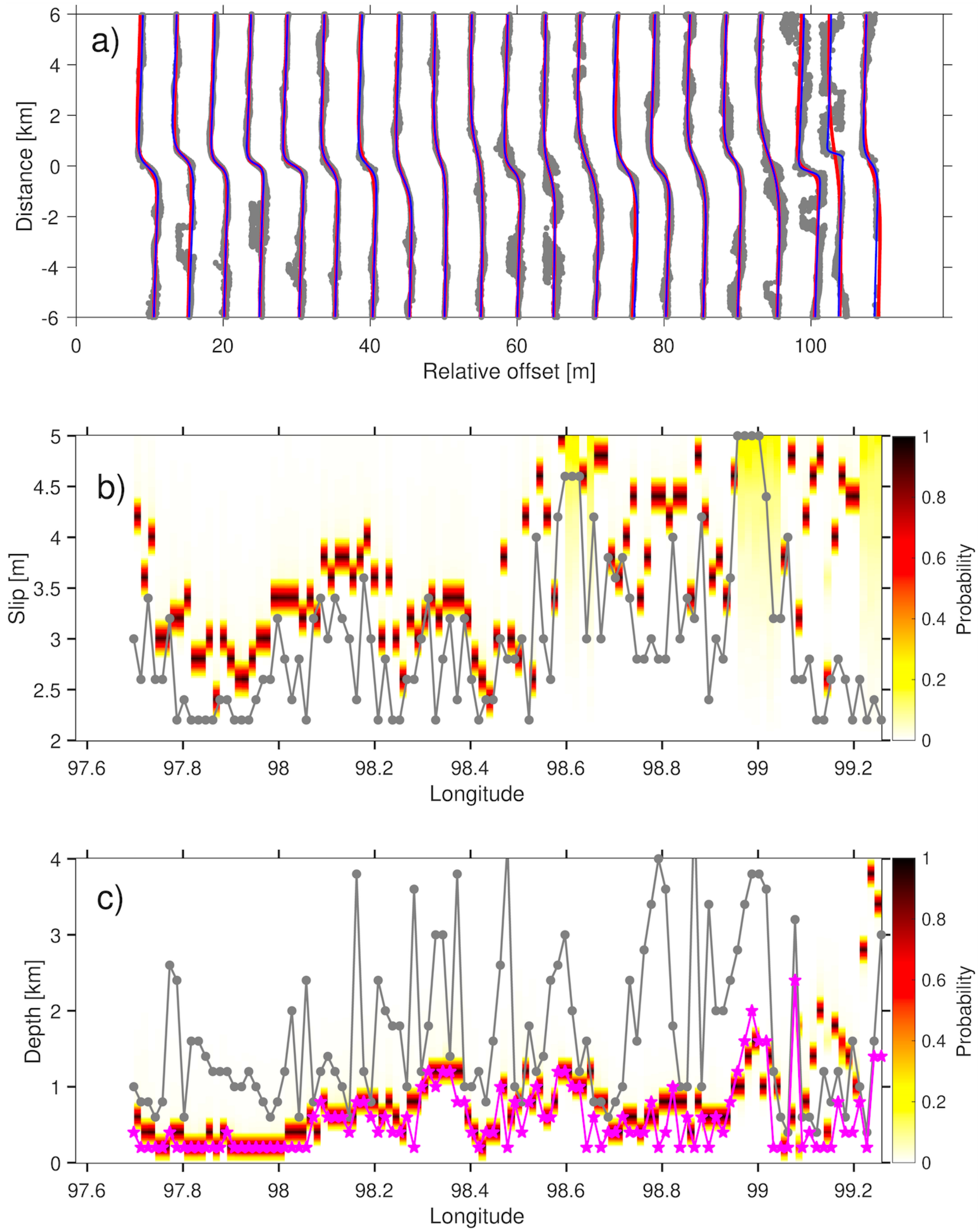

Figure 7. Data fitting and inversion results of the buried slip model. (a) Twenty-one examples of fault-cross profiles (gray point clouds) and data fitting from two models without (red lines) and with tapered shallow slip (blue lines). The profiles are arbitrarily shifted by an offset along the horizontal axis to aid in clear visualization. For several profiles, the red and blue lines are significantly overlapped and visually indistinguishable, indicating an almost identical level of data fitting. (b) Probability distribution for shallow coseismic slip (s) in the buried slip model. Gray dots are best-fitting values of the constant slip in the buried 2D slip model incorporating tapered shallow slip. (c) Probability distribution for the upper dislocation depth (d_2) of the buried slip model. Gray dots present the best-fitting values of d_2 in the buried slip model incorporating tapered shallow slip, and magenta stars denote the best-fitting values of d_3.

4.4 OFD and fault zone width during the Maduo earthquake

The OFD describes the processes related to distributed deformation in the near-field of the fault arising from inelastic deformation, including distributed brittle deformation (i.e., slip on subsidiary faults and fractures) and plastic yielding (i.e., cataclastic flow) (e.g., **Brooks et al., 2017; Kaneko and Fialko, 2011**). Our foregoing buried slip models imply that the reduced and progressively vanished slip in the near surface owing to a buried slip front would produce apparent OFD without needing to invoke plastic failure or secondary faulting (**Fig. S10**) to produce the observed surface displacement gradients. Based on the limited dataset of surface offset measurements in the field (**Fig. 9a**), we still can make a qualitative argument that the OFD during the Maduo earthquake is relatively high along surface-breaking segments (50%-70%, **Fig. 9a, 9b**). Our OFD calculations in conjunction with the abundant observations of significant, widespread ground cracks (**Fig. 2a**) and near-field rotations (**Fig. 6**), provide direct evidence that the OFD observed during the Maduo earthquake is prominent and highly variable over the whole length of the rupture.

We find that the shear zone width (derived from **Equations 1 and 2**; data-model fitting shown in **Fig. S10**) is overall consistent (400-1200 m) throughout the rupture, which is systematically anti-correlated with the width estimated from 0.2% of the shear strain intensity (**Fig. 9c, 9d**). The estimated two types of width above are comparable or smaller than the first type of crack (500-1500 m), which is associated with the continuous primary fault zone and trackable in the field (blue lines in **Fig. 2a**), but substantially narrower than the distribution of the second type of crack (typically >1 km, **Fig. 9c**). The fault zone width also exhibits correlation with the magnitude of total displacement, but no well-determined correlation with OFD (**Fig. 10**), implying that the near-fault surface displacement gradients are similar for both small and large horizontal offsets (**Fig. 10**).

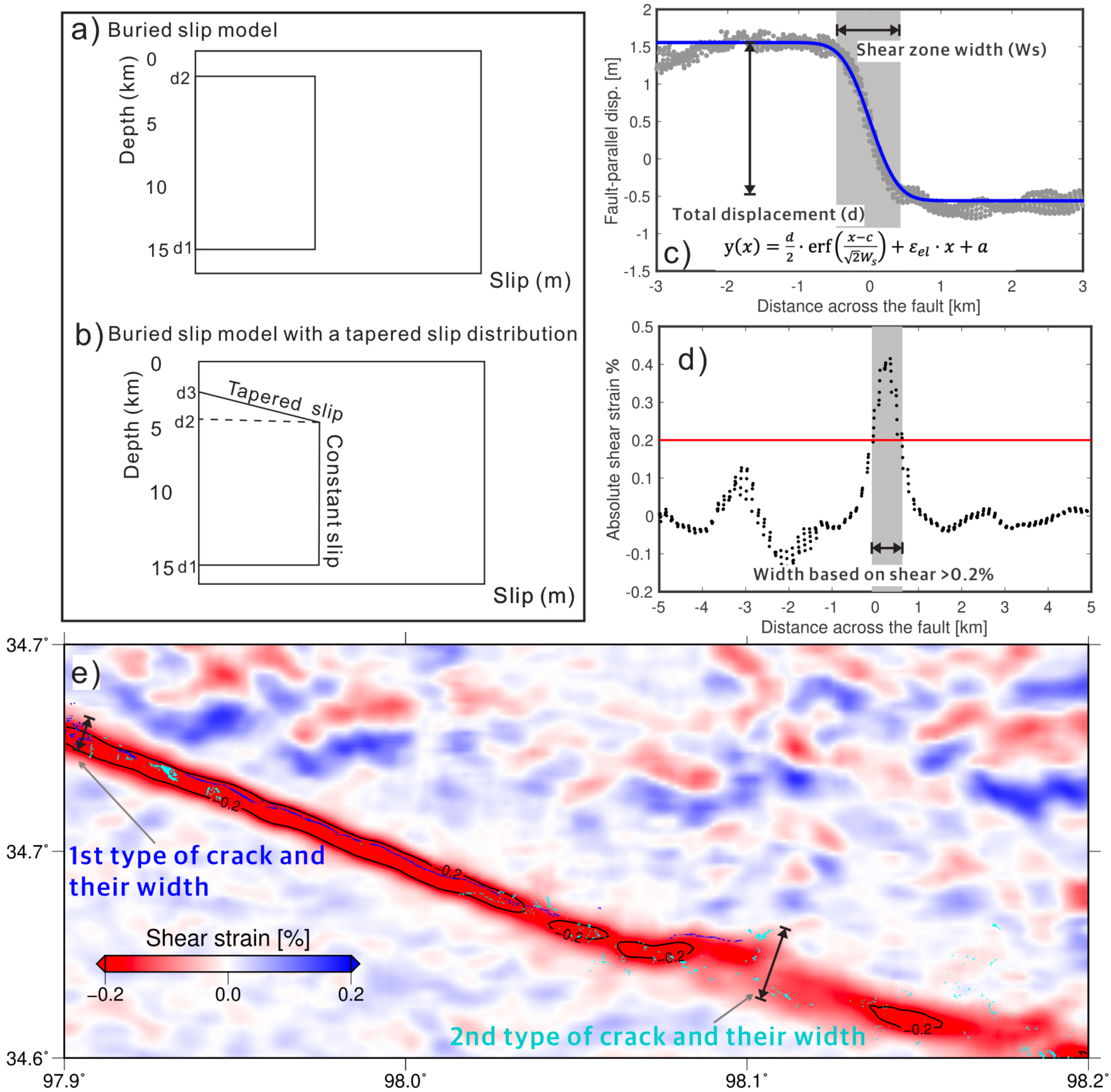

Figure 8. (a, b) Schematic illustration of the difference of the buried slip model without and with incorporating a tapered slip distribution. (c) Example of shear zone width and total displacement measurements (gray dots) fit with Equation 1 (blue lines). (d) Example of width measurements based on shear strain (>0.2%). (e) Example of width measurements of the first (blue) and second (cyan) type of cracks superimposed on the shear strain map saturated at ±0.2%. Black lines demonstrate 0.2% contours of shear strain.

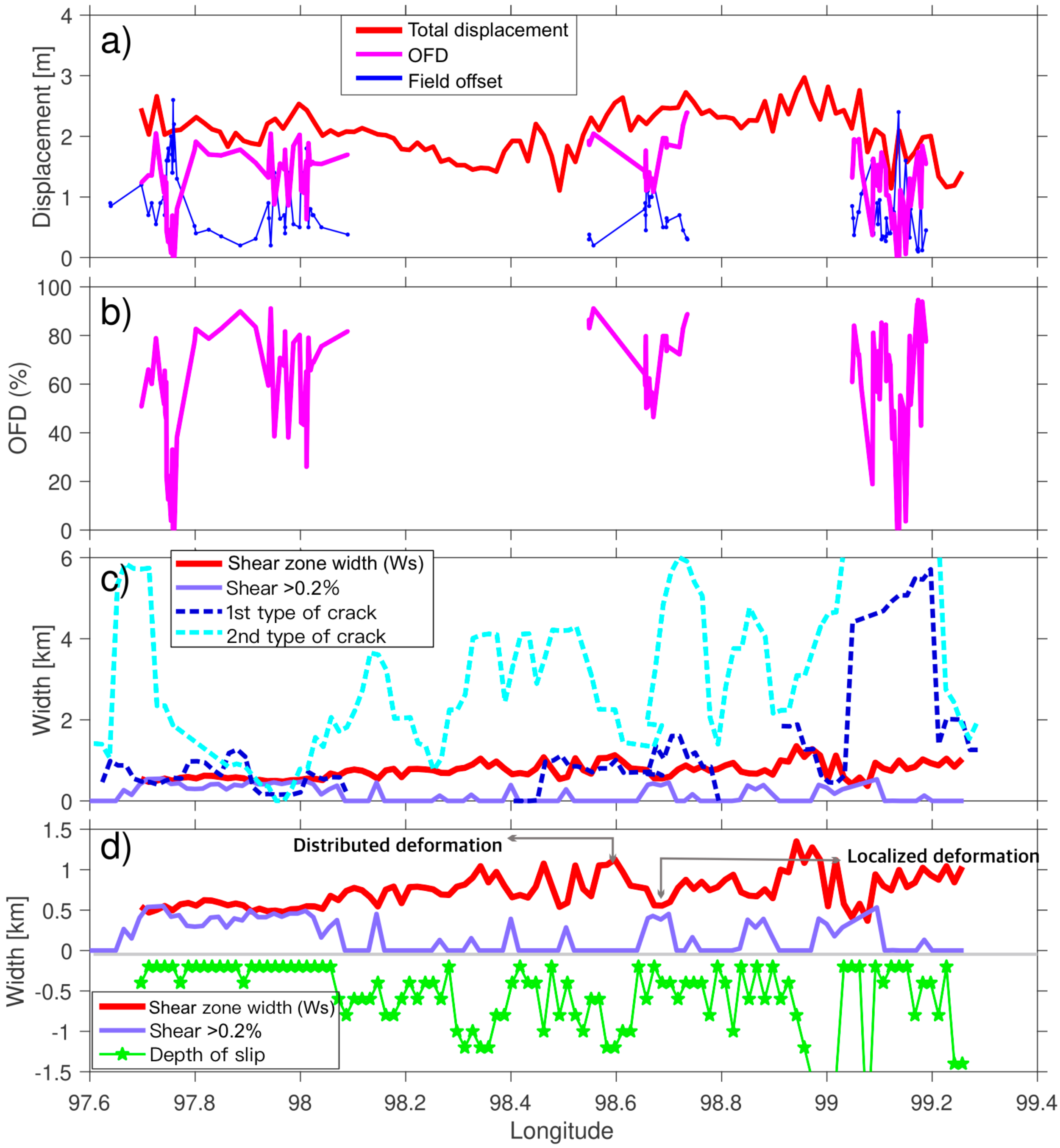

Figure 9. Total displacement (T in **Equation 1**), off-fault deformation (OFD) and shear zone width during the Maduo earthquake, calculated from a series of fault-parallel displacement profiles. (a) Comparison of total displacement (red line) and fault-parallel offset (blue line) measured by the field investigations after the earthquake. Quantification of OFD (purple line) is achieved by the difference of total displacement and coseismic fault-parallel offset from field investigation (assumed to be on-fault displacement). (b) Distribution of OFD as percentage of total displacement (OFD%). (c) Shear zone width (red line, W_s is **Equation 1**) and comparison with the width >0.2% of the shear strain intensity (purple line) and the cross-fault extent of two types of ground crack zone (blue and cyan dashed lines). (d)

Shear zone width (red line) and comparison with the depth of up-dip limit of tapered subsurface slip d3 (green lines, same as magenta stars shown in **Fig. 7c** but with a negative depth value for clear visualization). See examples in **Fig. 8**.

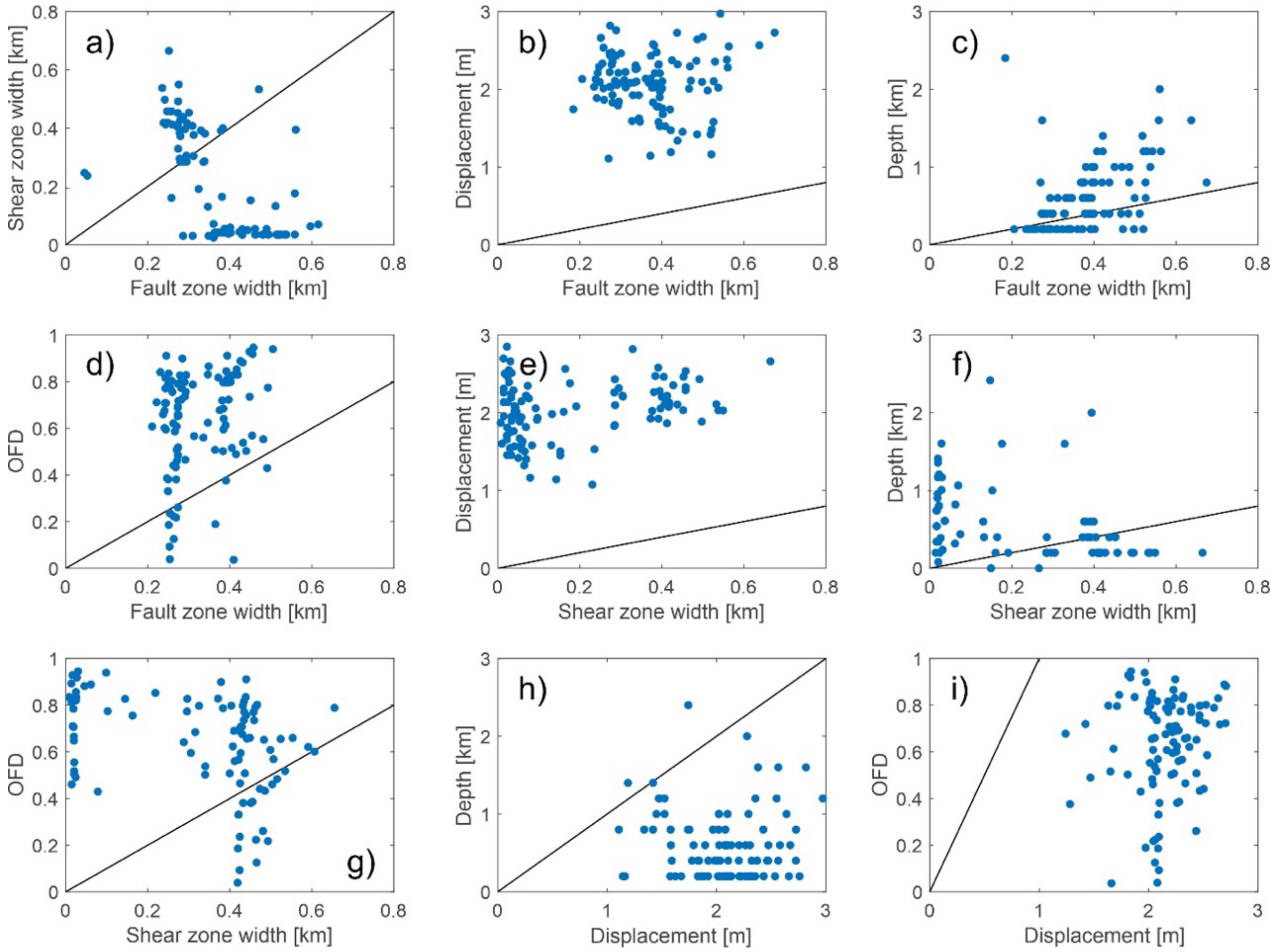

Figure 10. Comparison of fault zone width, shear width, total displacement, off-fault deformation and the depth of up dip limit of the coseismic slip. Black line: 1:1 line.

4.5 Distribution of coseismic slip and afterslip

Our newly-derived coseismic slip models are shown in **Fig. 11a-11c**. Comparison between three slip models and models from previous studies (**Fig. 11d-11f**) confirms multiple peak slip patches at depth during the Maduo earthquake. The size (~10-25 km) of slip patches bolsters the argument of **Klinger (2010)** that points to the similarity between the size of deep concentrated slip patches during earthquakes and the characteristic length of the ruptured fault segments (~15-25 km). Therefore, the segmentation of coseismic slip during the Maduo earthquake is a reliable characteristic resolved by various geodetic observations on the surface. The first-order consistency of three coseismic slip models and the published models, but still having some differences, attests to the fact that model parameterization and regularization during the inversion impact the resultant slip models but all lead to satisfactory data fitting (**Figs. S11-S13**) and similar residuals. All coseismic slip models are characterized by reduced coseismic slip close to the surface (0-4 km), and the peak slip (4-6 m) appears in the depth interval between 6 and 12 km. The SSD reflected by the slip models is in rough accordance with our previous buried slip models (**Fig. 7**). We note that studies of the Maduo earthquake benefit from high-quality multi-perspective observations of both InSAR and optical imagery (**Fig. 3**).

In contrast to the study of **Jin and Fialko (2021, Fig 11d)**, we preserve relatively dense coverage of InSAR observations in the near-field of the fault (<50 km) on both satellite tracks. Our comparison between InSAR and optical images supports the robustness of the InSAR observations in both near- and far-field (**Fig. S6**). Hence, data completeness in the vicinity of the fault does not appear to substantially reduce the apparent SSD in the slip inversion (e.g., **Xu et al., 2016**). We argue that the strong SSD (30%-60% depending on the segment) is a reliable feature of the Maduo earthquake despite the degree of smoothing applied in our models and previously published slip models.

The cumulative afterslip distribution is displayed in **Fig. 11g**. We find a striking complementary pattern between coseismic slip and afterslip distributions. The peak afterslip is 4-6 cm at a depth of 16-20 km. The majority of afterslip occurred in the periphery of the concentrated coseismic slip area and the afterslip region may highlight sections of the fault with rate strengthening properties. The peak amplitude of afterslip on the fault (within 6 months after the earthquake) is estimated to be less than 10% of the maximum amplitude of coseismic slip and the geodetic moment of the afterslip is only 4.6% of the coseismic. We did not impose additional constraints or damping on the coseismically ruptured areas, and only limited updip afterslip is captured by our postseismic InSAR measurements. The shallowest afterslip (at depths of <4 km) is estimated to be 20-30 cm; therefore, early updip afterslip is not sufficient to compensate for the apparent SSD. Due to the fact that the viscoelastic relaxation in a deep shear zone and/or lower crust is not considered in the inversion, the widespread downdip afterslip is likely over-estimated. A longer period of observation and more advanced modeling incorporating both afterslip and viscoelastic relaxation (e.g., **Zhao et al., 2021**) are required to better explain the long-term postseismic deformation at depth.

502

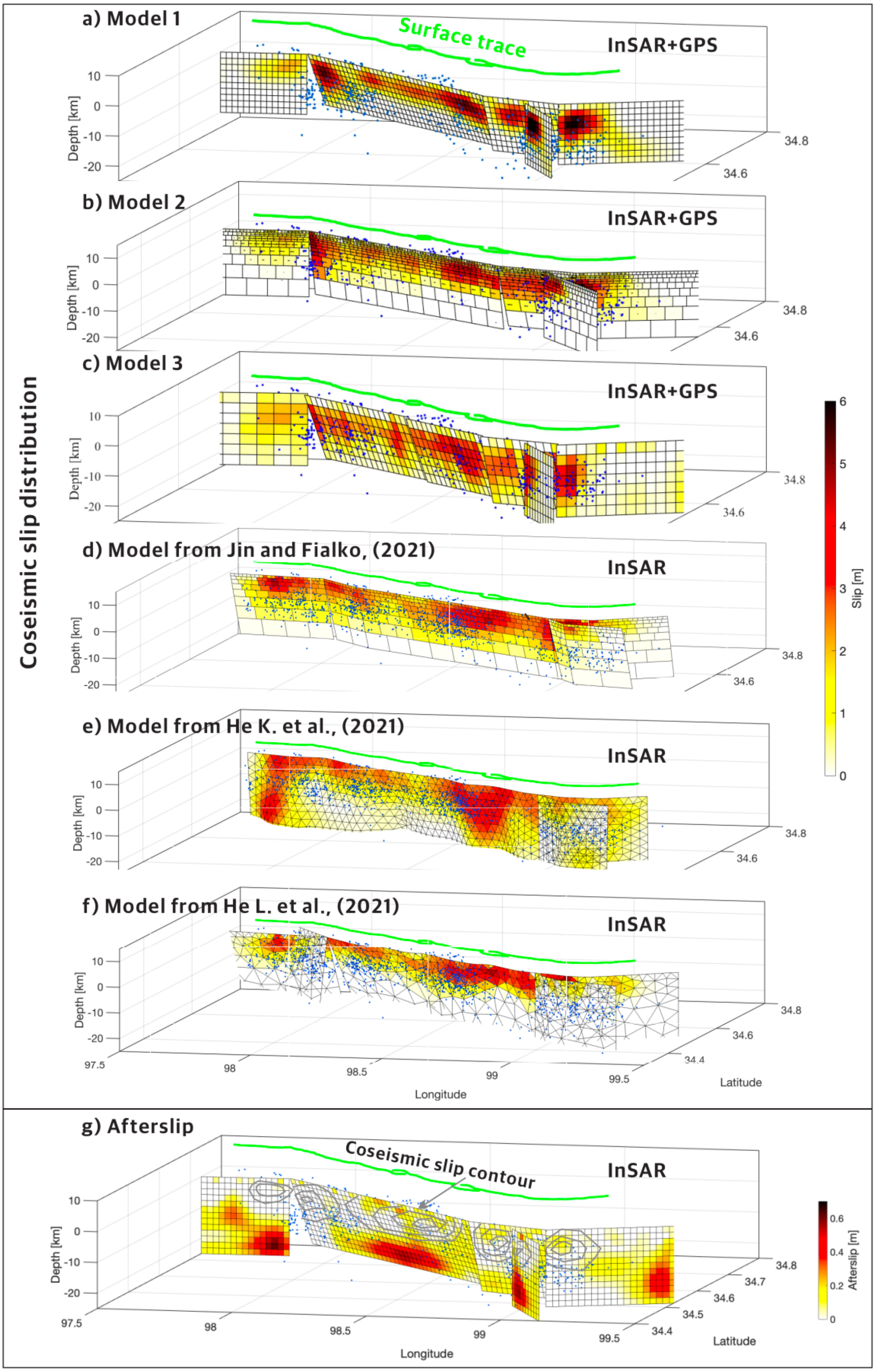

503 **Figure 11**. Coseismic (a-f) and afterslip (g) distributions of the 2021 Maduo earthquake. Green lines indicate surface

ruptures of the earthquake. The results highlight the complementary distributions of coseismic slip and afterslip.

5. Discussion

5.1 Coseismic fault damage and surface inelasticity linked to fault zone structure

The general picture of a fault zone is typically depicted as a nested hierarchical architecture, in which fault cores are enveloped by an inner and outer (wider) damage zone (e.g., **Chester et al., 1993; Faulkner et al., 2010; Perrin et al., 2016**). Our analysis of relocated aftershocks and geodetic observations provides a macroscopic description of fault structure for the Maduo earthquake, at a resolution that can be directly compared to the geological studies using field observations of exhumed faults. Our estimated value of the damage decay exponent (~0.5-1) based on aftershocks and coseismic surface geodetic observations is generally consistent with geological measurements on small and discrete faults at a millennial scale (~0.8; **Savage and Brodsky, 2011**), which represent long-term fault damage and co-existing healing processes over multiple earthquake cycles. The obtained consistency reflects distributed fault damage during the earthquake cycle and implies that dynamic earthquake ruptures play a key role in fault zone growth and evolution. The lower bound of our estimates (obtained along the western segment of the fault) also roughly agrees with the analysis of aftershock density decay of the 2019 Ridgecrest earthquake, despite a difference in methodology (~0.55 by **Rodriguez Padilla et al., 2022**).

However, the DDZT estimated for the Maduo earthquake based on the distribution of aftershocks around the rupture potentially represents both the width of the fault core and inner and outer damage zone (even some secondary strands), which cannot be directly compared to the fault damage zone width based on the geological estimates for low-offset immature faults (<25 km, **Perrin et al., 2016; Savage and Brodsky, 2011**). Although it is possible that dynamic effects may trigger seismicity in far broader outer damage zones and on some secondary strands leading to overprinting of multiple loci of fracturing, the systematically constant damage decay exponent (~0.5-1) implies that most of these secondary faults are still confined in the width of outer damage zones. We speculate another possible factor leading to the large damage zone thickness is the relatively fast healing process for the slowly-slipping (<4 mm/yr) immature causative faults. For the causative fault hosting the Maduo earthquake, it may slip at a rate of <2 mm/yr during the interseismic period based on geodetic observations (e.g., **Zhu et al. 2021**). For immature faults, the low level and distributed fault damage is likely accompanied by a relatively rapid healing process after an earthquake (**Perrin et al., 2016**). As a result, the fault will exhibit a low level of localization during its incipient growth stage. That may provide a plausible explanation for the discrepancy between our estimate of DDZT and the geological studies on the fault damage zone width, given that geologic datasets not likely include sparsely distributed fault zone damage >10 km from a primary fault (**Savage and Brodsky, 2011**).

The surface inelasticity during the Maduo earthquake has been recognized as a manifestation of deformation within the inner damage zone surrounding the seismogenic fault (e.g., **Cheng and Barnhart, 2021**), but the measured width of the inelastic deformation zone during earthquakes is highly sensitive to the resolution of datasets (**Rodriguez Padilla et al., 2022**). We note that the width of the inelastic deformation zone exceeding ±0.5% (even ±0.2% and may include elastic strain) shear strain is limited during the Maduo earthquake. The result could suggest an insignificant permanent (inelastic) yielding of the fault zone materials during the rupture. However, the limited permanent damage may be inherently consistent with the resolved buried slip front along several fault sections at shallow depths (0-4 km) obtained in this study, since a conspicuous tradeoff between elastic deformation of a buried slip front and shallow diffuse/plastic deformation may exist (e.g., **Nevitt et al., 2020**). We suspect that the weak, unconsolidated near-surface materials may have already been densely fractured and may have undergone considerably yielding by several historical ruptures. As a consequence, the buried slip front is capable of generate shallow diffuse/plastic deformation but with a limited footprint of permanent deformation within the inner damage zone.

Previous studies argue that the width of inelastic strain correlates with the net slip accumulated in fault evolution history (fault structural maturity) rather than the slip distribution in single earthquakes (e.g., **Cheng and Barnhart, 2021**). We infer that shallow buried slip fronts may be quite common on large earthquakes (M~7) that occurred on immature fault segments or on faults that are covered by thick young sedimentary units. The small gradient of surface offset produces limited surface inelasticity, especially in an immature fault zone lacking a well-developed and weakened gouge zone.

Our discussion above provides a comprehensive perspective of the evolution of the fault zone structure during the Maduo earthquake. We speculate that the seismogenic fault of the Maduo earthquake is most likely an incipient fault which is experiencing a progressive process of fault-zone evolution, in which the fault has complex geometrical variation, a wide outer damage zone, a poorly developed inner damage zone and limited coseismic surface inelasticity.

5.2 Strain budget of the immature fault

Our coseismic and postseismic observations along with the observed strong SSD have implications for the strain budget of the causative fault of the Maduo earthquake. Our postseismic observations document the limited geodetic moment released by afterslip, mostly by down-dip afterslip. The low released moment ratio of afterslip to coseismic slip (< 10%) reflects structural immaturity (e.g., **Li et al., 2020**), which is also consistent with a global compilation of the geodetically derived postseismic to coseismic moment release (**Wimpenny et al., 2017**). Given that we did not consider the potential contribution from viscoelastic relaxation in the lower crust, the estimated moment ratio of afterslip to coseismic slip represents an upper bound. Compared to the rapid shallow afterslip observed on some structurally mature faults with a well-developed shallow gouge zone featuring strong rate-strengthening properties (e.g., **Floyd et al., 2016**), the afterslip in the aftermath of the Maduo earthquake is relatively slow and spatially limited. Our postseismic timeseries suggest that the low post- to co-seismic moment ratio is reliable based on a well constrained logarithmic extrapolation of the displacement time-series (**Fig. 3**) back to the time of the earthquake. We infer that only minor (0.5–2 cm) LOS displacement occurred due to early moment release immediately after the earthquake (4 days), which is not captured by the postseismic InSAR observations.

Furthermore, **Zhao et al. (2021)** document a low (undetectable by geodetic observations, <2 mm/yr based on **Zhu et al., 2021**) shear strain rate from InSAR measurements and no detectable interseismic shallow fault creep prior to the Maduo earthquake spanning 2015-2020. This could point to the absence of ductile shear zones below immature low-slip-rate and low-offset causative faults, likely resulting in broadly distributed strain at the surface late in the earthquake cycle (**Hearn et al., 2015**). Another, potentially important factor that may contribute to the interseismically distributed strain across immature faults is the development of permanent, off-fault deformation. Such inference has been supported by geologic investigations (significant discrepancy between geodetic and geologic slip rates) and a vast body of modelling work. For instance, **Shelef and Oskin (2010)** suggest that ~23% of the total fault slip rate is absorbed via distributed off-fault strain about the moderately mature Calico fault (9.6 km of net slip) compared with 31%-46% of the total strain accommodated by off-fault deformation on the less mature Harper Lake fault (3.5 km of net slip). **Herbert et al. (2014)** document that distributed, off-fault deformation could account for 40% ± 23% of the total strain across the most immature, disconnected faults within the Mojave Desert area of the eastern California shear zone. Significant amounts of permanent strain about immature faults may bias fault slip-rate estimates and may control earthquake rupture, fault behavior and long-term fault propagation (e.g., **Dolan and Haravitch, 2014; Perrin et al., 2016**).

During the coseismic rupture, the fault hosting the Maduo earthquake exhibited a strong SSD, which cannot be fully recovered by the limited afterslip and potential interseismic creep, although it is challenging to geodetically quantify any low-magnitude aseismic surface creep (<2-3 mm/yr) during the interseismic period. Rather, the significant SSD is largely compensated by distributed OFD during earthquake ruptures. SSD on strike-slip faults is potentially magnitude dependent and is most often found for earthquakes of Mw <7.5. **Lauer et al. (2020)** compared slip models of various earthquakes and found that no SSD can be identified for major events with Mw>7.5, such as the 2001 Mw 7.8 Kokoxili earthquake, the 2002 Mw 7.9 Denali earthquake, or the 2013 Mw 7.7 Baluchistan earthquake. These large earthquakes commonly occurred on long (large-scale), fast-slipping, ancient and structurally mature faults (**Perrin et al., 2016**). In addition, the degree and extent of the SSD have been linked to the cumulative fault displacement in the study of **Dolan and Haravitch (2014)**. The authors indicate that larger SSDs tend to emerge on less mature and incipient faults (net fault slip <25 km) based on a global compilation of surface and deep fault slip during earthquakes. Accordingly, the fault hosting the Maduo earthquake could be considered to be a young fault with poorly developed fault structures, which results in broadly distributed near-surface brittle damage during coseismic ruptures.

In the case of buried faulting typically observed on young faults, the OFD may be insignificant dependent on the burial depth of the slip front and the constitutive parameter of the host rocks (i.e., Young's modulus, Poisson's ratio, etc.) of the shallowest portion of the faults. Accordingly, the observed OFD from near-field geodesy cannot reasonably account for the apparent SSD, such as the documented buried slip during the 2014 Mw6.0 South Napa earthquake (e.g., **Brooks et al., 2017**). **Nevitt et al. (2020)** examine the effects of lithospheric layering, elastoplasticity and reduced elastic stiffness in the densely-fractured compliant zone on surface displacement, subsurface slip and fault behavior. They suggest that the layering of elastic properties and/or elastoplasticity play an important role in controlling the fault behavior of the buried fault tip. They find that layered models incorporating a stiffer basement and a softer, unconsolidated shallow alluvium could generate steep slip gradients with off-fault inelastic strain surrounding the buried tip. Addition of elastoplasticity will enhance the near-surface slip gradient.

We suggest that OFD is not a unique factor that can account for the apparent SSD during a specific earthquake with both surface-breaking and buried slip on the immature fault. Our analysis demonstrates a mixed-mode of surface-breaking and buried slip throughout the whole rupture, which may be common for an M~7 earthquake (**Yuan et al., 2022**). Alternatively, the inferred SSD could stem from distributed coseismic brittle damage in the uppermost portion of the incipient fault, which represents a compliant fault zone. To estimate the rigidity decrease arising from coseismic fracturing in the volume of rock surrounding the primary fault, we constrain the ratio of elastic shear modulus of the compliant zone (μ_1) and the surrounding crust (μ_2), μ_1/μ_2, for the Maduo earthquake using an analytical two-dimensional buried slip model with consideration of the compliant zone (**Text S3**). Our result suggests that the ratio, μ_1/μ_2, is about 0.17-0.3 and the width of the compliant zone is ~1 km (**Fig. S9**). Overall, our estimate here is roughly consistent with the analysis of **Rodriguez Padilla et al. (2022)** for the Ridgecrest earthquake, although our data resolution and approach do not allow for the estimation of a spatially varying rigidity reduction across the main rupture trace.

During the interseismic period, the irrecoverable damage originating from dynamic yielding during rupture may be compounded by enhanced interseismic strain rates during long-term localization of fault (**Perrin et al., 2016**). Such an inference is consistent with the study by **Lindsey, Fialko, et al. (2014)** based on interseismic geodetic observations. They suggest that the enhanced interseismic strain rates on mature fault could reduce fault yield strength leading to unrecoverable distributed fault-zone damage, whilst this effect is potentially limited for immature fault zone. In other works, while a fault zone localizes as it matures and accelerates, it may also become more damaged and thus behave more compliantly than an immature fault. This implies that coseismic earthquake damage plays an important role in long-term fault growth. Distributed near-fault damage facilitates localization of elastic deformation into fault zones and may act as shear strain sink over long timescales.

6. Conclusion

In this study, we explored a comprehensive dataset associated with the 2021 Mw7.4 Maduo earthquake to investigate coseismic and postseismic deformation, underlying processes and their relationships, the thickness of fault damage zones, damage density decay, shallow slip deficit, off-fault deformation, and near-surface inelasticity. Compared to previous studies of the Maduo earthquake, our investigation provides a more comprehensive quantification of the kinematics of the causative fault, reveal several valuable aspects of deep and surface fault-zone deformation, and has important implications for the earthquake cycle behavior and long-term evolution of fault structure of low-offset incipient faults, which are widely distributed in the interior of the Tibetan plateau. Our primary findings and conclusions are summarized as follows:

1. Postseismic InSAR observations from PS timeseries analysis reveal the spatially limited afterslip distribution, especially up dip of the coseismically ruptured patches. Kinematic inversion for afterslip demonstrates a complementary distribution between down-dip afterslip and coseismic peak-slip regions. A small ratio of post- to coseismic moment release (<10%, and only very little shallow afterslip) is indicated for the Maduo earthquake.

2. We calculate the thickness of the fault damage zone and damage decay exponent using the relocated aftershocks. We suggest that the Maduo earthquake produced a wide damage zone (6-18 km), albeit with a systematic

variation along the rupture. The estimated damage decay exponent (0.5-1) is generally consistent with previous geological studies (~0.8, representing long-term deformation), suggesting distributed fault damage during the earthquake cycle.

3. The Maduo earthquake generated localized shear strain and rotations but lacks significant dilatational strain, revealed by high-resolution displacement fields using sub-pixel correlation of optical imagery. The magnitude of shear and dilatational strain is mostly less than 0.2% yield strain derived from rock mechanics studies, indicating insignificant surface inelasticity during the Maduo earthquake. The width of co-seismic inelastic deformation (0.2% yield strain) does not correlate with variations in total displacement, the depth of buries slip front and the OFD.

4. In conjunction with the three-dimensional coseismic slip model, we also note a pronounced SSD during the Maduo earthquake. Using a two-dimensional buried slip model, we observe a mixed mode of surface-breaking rupture and a buried near-surface slip front throughout the entire rupture of the Maduo earthquake. The buried near-surface slip front along several fault sections could introduce a fault-parallel displacement gradient across the fault without invoking OFD. Based on the offset measurements in the field along surface-breaking segments (on-fault displacement), we infer considerable OFD (40%-80%). The substantial OFD is likely pervasive along the whole rupture considering the widely distributed ground cracks.

Data Availability Statement

The Sentinel-1 data are made available by the ESA and distributed and archived through the Alaska Satellite Facility (ASF) (https://www.asf.alaska.edu/sentinel/). The GPS data, surface cracks and relocated aftershocks can be found in literature cited in the main text. The moment tensor solutions come from the U.S. Geological Survey (USGS; http://earthquake.usgs.gov), the Global Centroid Moment Tensor project (CMT; http://www.globalcmt.org) and the China Earthquake Data Center (CEDC, http://data.earthquake.cn/index.html).

Acknowledgement

This research was supported by the Basic Scientific Funding of Institute of Geology, China Earthquake Administration (IGCEA2138, IGCEA2104, IGCEA1809), the National Key Laboratory of Earthquake Dynamics (LED2019A02), the National Natural Science Foundation of China (42174009,41872229), the National Nonprofit Fundamental Research Grant of China, Institute of Geology, China, Earthquake Administration (IGCEA2005).

Reference:

Amey, R. M. J., Hooper, A., & Walters, R. J. (2018). A Bayesian method for incorporating self-similarity into earthquake slip inversions. Journal of Geophysical Research: Solid Earth, 123(7), 6052-6071.

Antoine, S. L., Klinger, Y., Delorme, A., Wang, K., Bürgmann, R., & Gold, R. D. (2021). Diffuse deformation and surface faulting distribution from submetric image correlation along the 2019 Ridgecrest, California, ruptures. Bull. Seismol. Soc. Am., (5), 2275-2302.

Barnhart, W. D., Gold, R. D., & Hollingsworth, J. (2020). Localized fault-zone dilatancy and surface inelasticity of the 2019 Ridgecrest earthquakes. Nature Geoscience, 13(10), 699-704.

Ben-Zion, Y. (2008). Collective behavior of earthquakes and faults: Continuum-discrete transitions, progressive evolutionary changes, and different dynamic regimes. Reviews of Geophysics, 46(4).

Ben-Zion, Y., & Zhu, L. (2002). Potency-magnitude scaling relations for southern California earthquakes with 1.0< M L< 7.0. Geophysical Journal International, 148(3), F1-F5.

Brooks, B. A., Minson, S. E., Glennie, C. L., Nevitt, J. M., Dawson, T., Rubin, R., et al. (2017). Buried shallow fault slip from the South Napa earthquake revealed by near-field geodesy. Science advances, 3(7), e1700525.

Chester, F. M., Evans, J. P., & Biegel, R. L. (1993). Internal structure and weakening mechanisms of the San Andreas fault. Journal of Geophysical Research: Solid Earth, 98(B1), 771-786.

Cheng, G., & Barnhart, W. D. (2021). Permanent Co-Seismic Deformation of the 2013 Mw7. 7 Baluchistan, Pakistan Earthquake From High-Resolution Surface Strain Analysis. Journal of Geophysical Research: Solid Earth, 126(3), e2020JB020622.

Dolan, J. F., & Haravitch, B. D. (2014). How well do surface slip measurements track slip at depth in large strike-slip earthquakes? The importance of fault structural maturity in controlling on-fault slip versus off-fault surface deformation. Earth and Planetary Science Letters, 388, 38-47.

Fialko, Y. (2004). Probing the mechanical properties of seismically active crust with space geodesy: Study of the coseismic deformation due to the 1992 Mw7. 3 Landers (southern California) earthquake. Journal of Geophysical Research: Solid Earth, 109(B3).

Faulkner, D. R., Mitchell, T. M., Jensen, E., & Cembrano, J. (2011). Scaling of fault damage zones with displacement and the implications for fault growth processes. Journal of Geophysical Research: Solid Earth, 116(B5).

Faulkner, D. R., Jackson, C. A. L., Lunn, R. J., Schlische, R. W., Shipton, Z. K., Wibberley, C. A. J., & Withjack, M. O. (2010). A review of recent developments concerning the structure, mechanics and fluid flow properties of fault zones. Journal of Structural Geology, 32(11), 1557-1575.

Floyd, M. A., Walters, R. J., Elliott, J. R., Funning, G. J., Svarc, J. L., Murray, J. R., ... & Wright, T. J. (2016). Spatial variations in fault friction related to lithology from rupture and afterslip of the 2014 South Napa, California, earthquake. Geophysical Research Letters, 43(13), 6808-6816.

Guo, R., Yang, H., Li, Y., Zheng, Y., & Zhang, L. (2021). Complex Slip Distribution of the 2021 Mw 7.4 Maduo, China, Earthquake: An Event Occurring on the Slowly Slipping Fault. Seismological Research Letters.

Goodman, J., & Weare, J. (2010). Ensemble samplers with affine invariance. Communications in applied mathematics and computational science, 5(1), 65-80.

Hooper, A., Bekaert, D., Spaans, K., & Arıkan, M. (2012). Recent advances in SAR interferometry time series analysis for measuring crustal deformation. Tectonophysics, 514, 1-13.

He, L., Feng, G., Wu, X., Lu, H., Xu, W., Wang, Y., Liu, J., Hu, J., & Li, Z. Coseismic and early postseismic slip models of the 2021 Mw 7.4 Maduo earthquake (western China) estimated by space-based geodetic data. Geophysical Research Letters, e2021GL095860.

He, K., Wen, Y., Xu, C., & Zhao, Y. (2021). Fault Geometry and Slip Distribution of the 2021 Mw 7.4 Maduo, China, Earthquake Inferred from InSAR Measurements and Relocated Aftershocks. Seismological Research Letters.

Hearn, E. H., and W. R. Thatcher (2015), Reconciling viscoelastic models of postseismic and interseismic deformation: Effects of viscous shear zones and finite length ruptures, J. Geophys. Res. Solid Earth, 120, doi:10.1002/2014JB011361.

Herbert, J. W., Cooke, M. L., Oskin, M., & Difo, O. (2014). How much can off-fault deformation contribute to the slip rate discrepancy within the eastern California shear zone?. Geology, 42(1), 71-75.

Jin, Z., & Fialko, Y. (2021). Coseismic and early postseismic deformation due to the 2021 M7. 4 Maduo (China) earthquake. Geophysical Research Letters, 48(21), e2021GL095213.

Kaneko, Y., & Fialko, Y. (2011). Shallow slip deficit due to large strike-slip earthquakes in dynamic rupture simulations with elasto-plastic off-fault response. Geophysical Journal International, 186(3), 1389-1403.

Klinger, Y. (2010). Relation between continental strike-slip earthquake segmentation and thickness of the crust. Journal of Geophysical Research: Solid Earth, 115(B7).

Lauer, B., Grandin, R., & Klinger, Y. (2020). Fault geometry and slip distribution of the 2013 Mw 7.7 Balochistan earthquake from inversions of SAR and optical data. Journal of Geophysical Research: Solid Earth, 125(7), e2019JB018380.

Lockner, D. A. (1998). A generalized law for brittle deformation of Westerly granite. Journal of Geophysical Research: Solid Earth, 103(B3), 5107-5123.

Li, Y., Bürgmann, R., & Zhao, B. (2020). Evidence of Fault Immaturity from Shallow Slip Deficit and Lack of Postseismic Deformation of the 2017 Mw 6.5 Jiuzhaigou Earthquake. Bulletin of the Seismological Society of America, 110(1), 154-165.

Lindsey, E. O., Sahakian, V. J., Fialko, Y., Bock, Y., Barbot, S., & Rockwell, T. K. (2014). Interseismic strain localization in the San Jacinto fault zone. Pure and Applied Geophysics, 171(11), 2937-2954.

Lindsey, E. O., Fialko, Y., Bock, Y., Sandwell, D. T., & Bilham, R. (2014). Localized and distributed creep along the southern San Andreas Fault. Journal of Geophysical Research: Solid Earth, 119(10), 7909-7922.

Manighetti, I., Caulet, C., De Barros, L., Perrin, C., Cappa, F., & Gaudemer, Y. (2015). Generic along-strike segmentation of A far normal faults, East Africa: Implications on fault growth and stress heterogeneity on seismogenic fault planes. Geochemistry, Geophysics, Geosystems, 16(2), 443-467.

Milliner, C., Donnellan, A., Aati, S., Avouac, J. P., Zinke, R., Dolan, J. F., Wang, K., & Bürgmann, R. (2021). Bookshelf Kinematics and the Effect of Dilatation on Fault Zone Inelastic Deformation: Examples From Optical Image Correlation Measurements of the 2019 Ridgecrest Earthquake Sequence. Journal of Geophysical Research: Solid Earth, 126(3), e2020JB020551.

Nevitt, J. M., Brooks, B. A., Catchings, R. D., Goldman, M. R., Ericksen, T. L., & Glennie, C. L. (2020). Mechanics of near-field deformation during co-and post-seismic shallow fault slip. Scientific reports, 10(1), 1-13.

Perrin, C., Manighetti, I., Ampuero, J. P., Cappa, F., & Gaudemer, Y. (2016). Location of largest earthquake slip and fast rupture controlled by along-strike change in fault structural maturity due to fault growth. Journal of Geophysical Research: Solid Earth, 121(5), 3666-3685.

Powers, P. M., & Jordan, T. H. (2010). Distribution of seismicity across strike‐slip faults in California. Journal of Geophysical Research: Solid Earth, 115(B5).

Rosen, P. A., Gurrola, E., Sacco, G. F., & Zebker, H. (2012, April). The InSAR scientific computing environment. In EUSAR 2012; 9th European Conference on Synthetic Aperture Radar (pp. 730-733). VDE.

Rosu, A.-M., Pierrot-Deseilligny, M., Delorme, A., Binet, R., & Klinger, Y. (2015). Measurement of ground displacement from optical satellite image correlation using the free open-source software MicMac. ISPRS Journal of Photogrammetry and Remote Sensing, 100, 48–59.

Rupnik, E., and Daakir, M., Pierrot-Deseilligny, M. (2017). MicMac - a free, open-source solution for photogrammetry. Open Geospatial Data Software & Standards, 2(1).

Rodriguez Padilla, A. M., Oskin, M. E., Milliner, C. W., & Plesch, A. (2022). Accrual of widespread rock damage from the 2019 Ridgecrest earthquakes. Nature Geoscience, 15(3), 222-226.

Savage, H.M., and Brodsky, E.E., 2011, Collateral damage: Evolution with displacement of fracture distribution and secondary fault strands in fault damage zones: Journal of Geophysical Research, v. 116, B03405, doi:10.1029/2010JB007665.

Savage, J. C., Burford, R. O. (1973). Geodetic determination of relative plate motion in central California. Journal of Geophysical Research, 78(5), 832-845.

Shelef, E., & Oskin, M. (2010). Deformation processes adjacent to active faults: Examples from eastern California. Journal of Geophysical Research: Solid Earth, 115(B5).

Taylor, M., and A. Yin (2009), Active structures of the Himalayan-Tibetan orogen and their relationships to earthquake distribution, contemporary strain field, and Cenozoic volcanism, Geosphere, 5(3), 199–214.

Tang, C. H., Hsu, Y. J., Barbot, S., Moore, J. D., & Chang, W. L. (2019). Lower-crustal rheology and thermal gradient in the Taiwan orogenic belt illuminated by the 1999 Chi-Chi earthquake. Science advances, 5(2), eaav3287.

Valoroso, L., Chiaraluce, L., & Collettini, C. (2014). Earthquakes and fault zone structure. Geology, 42(4), 343-346.

Waldhauser F. 2000. A double-difference earthquake location algorithm: Method and application to the Northern Hayward Fault, California. Bull Seismol Soc Am, 90: 1353–1368

Wang, R., Parolai, S., Ge, M., Jin, M., Walter, T. R., & Zschau, J. (2013). The 2011 M w 9.0 Tohoku earthquake: Comparison of GPS and strong-motion data. Bulletin of the Seismological Society of America, 103(2B), 1336–1347

Wang, M., Wang, F., Jiang, X., Tian, J., Li, Y., Sun, J., & Shen, Z. K. (2021). GPS determined coseismic slip of the 2021 Mw7.4 Maduo, China, earthquake and its tectonic implication. Geophysical Journal International, 228(3), 2048-2055.

Wang, W., Fang, L., Wu, J., Tu, H., Chen, L., Lai, G., & Zhang, L. (2021). Aftershock sequence relocation of the 2021 Ms7. 4 Maduo earthquake, Qinghai, China. Science China Earth Sciences, 64(8), 1371-1380.

Wang, M., Shen, Z. K. (2020). Present-Day Crustal Deformation of Continental China Derived from GPS and Its Tectonic Implications. Journal of Geophysical Research: Solid Earth, 125(2), e2019JB018774.

Wimpenny, S., Copley, A., & Ingleby, T. (2017). Fault mechanics and post-seismic deformation at Bam, SE Iran. Geophysical Journal International, 209(2), 1018-1035.

Xu, X., X. Tong, D. T. Sandwell, C. W. D. Milliner, J. F. Dolan, J. Hollingsworth, S. Leprince, and F. Ayoub (2016). Refining the shallow slip deficit, Geophys. J. Int. 204, no. 3, 1843–1862,

Yuan, Z., Li, T., Su, P., Sun, H., Ha, G., Guo, P., et al. (2022). Large surface-rupture gaps and low surface fault slip of the 2021 Mw 7.4 Maduo earthquake along a low-activity strike-slip fault, Tibetan Plateau. Geophysical Research Letters, 49, e2021GL096874.

Zhu, Y., Diao, F., Fu, Y., Liu, C., & Xiong, X. (2021). Slip rate of the seismogenic fault of the 2021 Maduo earthquake in western China inferred from GPS observations. Science China Earth Sciences, 64(8), 1363-1370.

Zhao, D., Qu, C., Chen, H., Shan, X., Song, X., & Gong, W. (2021). Tectonic and Geometric Control on Fault Kinematics of the 2021 Mw7. 3 Maduo (China) Earthquake Inferred From Interseismic, Coseismic, and Postseismic InSAR Observations. Geophysical Research Letters, 48(18), e2021GL095417.